

國立交通大學

電信工程學系碩士班 碩士論文

數位電視廣播接收機設計：演算法及基頻架構



DVB-T Receiver Design: Algorithms and
Baseband Architecture

研究生：黃俊傑

Student: Jun-Jue Huang

指導教授：蘇育德 博士

Advisor: Dr. Yu Ted Su

中華民國九十三年六月

數位電視廣播接收機設計：演算法及基頻架構

DVB-T Receiver Design:
Algorithms and Baseband Architecture

研究生：黃俊傑

Student : Jun-Jue Huang

指導教授：蘇育德 博士

Advisor : Dr. Yu T. Su

國立交通大學



A Thesis Submitted to
The Institute of Communication Engineering
College of Electrical Engineering and Computer Science
National Chiao Tung University
In Partial Fulfillment of the Requirements
For the Degree of Master of Science
In
Communication Engineering
June 2004

Hsinchu, Taiwan, Republic of China

中華民國九十三年六月

數位電視廣播接收機設計：演算法及基頻架構

研究生：黃俊傑

指導教授：蘇育德 博士

國立交通大學電信工程學系碩士班

摘要

歐規的數位影像廣播(DVB-T)系統使用了正交分頻多工(OFDM)的技術，在無線傳輸的通道下能提供高速率傳輸、高效率的頻譜使用率的多媒體服務及對抗頻率選擇的通道衰減。

本篇論文提出了一個可以工作在單頻網路(SFN)的數位影像廣播接收機(DVB-T receiver)的基頻架構。我們將會討論基頻信號處理單元的演算法。這些演算法包含時間與頻率同步、通道估計/等化器以及突波雜訊抑制(Impulse noise suppression)。此外我們還提出了利用決策重建及遞迴通道估計之抑制突波方法，通道估計的演算法能完全利用到時域及頻域的資訊。

我們透過電腦模擬來評估每個子系統的性能以及整體效能還有相對參數的最佳化。

DVB-T Receiver Design: Algorithms and Baseband Architecture

Student : Jun-Jue Huang Advisor : Dr. Yu T. Su

Institute of Communication Engineering
National Chiao Tung University

Abstract

To offer high-bit-rate high performance, bandwidth-efficient multimedia services and combat the inevitable frequency-selective fading, the European standard for terrestrial digital video broadcasting (DVB-T) has adopted the orthogonal frequency-division multiplexing (OFDM) technique for broadcasting over wideband wireless channels.

This thesis presents a baseband architecture and develop algorithms for various corresponding signal processing units for a single frequency network (SFN) DVB-T receiver. These algorithms serve the functionalities of time and frequency synchronization, channel estimation/equalization and impulse noise suppression. Among others, we propose a fast frequency synchronizer and a decision-aided algorithm for joint channel estimation and impulse noise suppression. The channel estimation part makes full use of the time and frequency correlation information. The performance of each subsystems and the overall system is evaluated through computer simulations and related parameters are optimized accordingly.

誌 謝

本論文得以順利完成，首先要感謝我的指導教授蘇育德教授，在這兩年的研究生生活中，無論在電信領域的專業或生活上的待人處世，都使我有很大收穫。也要感謝蒞臨的口試委員，他們提供的意見和補充資料使本文得以更加完整。此外，我要感謝聯發科技對本計畫的贊助，尤其李宗霖學長不時的提供寶貴意見與幫助。另外，實驗室學長陳彥志的鼎力相助、還有同學及學弟的幫忙勉勵，讓我在學業及研究上獲益匪淺

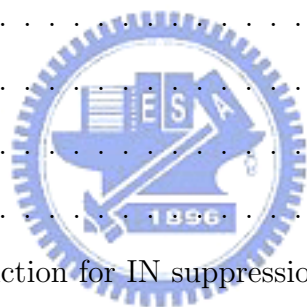
最後，要感謝的就是一直關心我鼓勵我的家人，他們使我在求學的過程中無後顧之憂，得以追求自己的目標，願他們永遠平安、幸福！

Contents

Chinese Abstract	i
Abstract	ii
Acknowledgements	iii
Contents	iv
List of Figures	vi
List of Tables	x
1 Introduction	1
1.1 DVB-T systems	3
2 Frequency and Timing Synchronization Subsystems	10
2.1 Joint coarse timing and fractional frequency offset estimation	10
2.1.1 Coarse timing recovery in multipath fading channels	14
2.2 Coarse frequency synchronization	15
2.2.1 Improved coarse frequency synchronization	18
2.3 Timing tracking	19
2.4 Computational complexity	22
2.5 Numerical Behavior	23



3	Channel Estimation	26
3.1	Fundamental of OFDM Channel Estimate	26
3.2	DVB-T channel model	29
3.2.1	Jakes model	30
3.3	Phase compensation	30
3.4	Transform-domain channel estimation algorithm	32
3.4.1	Cutoff frequency	33
3.5	Model-based channel estimation	35
3.6	2-D model-based channel estimate with transform-domain processing . .	38
3.7	Computational complexity	39
3.8	Numerical examples	40
4	Impulse Noise Suppression	44
4.1	Background	44
4.2	Impulse noise model	44
4.3	Impulse noise detection	46
4.4	Blanking method	46
4.5	Decision-aided reconstruction for IN suppression (DARINS)	47
4.6	Iterative channel estimation using DARINS	50
4.7	Viterbi approach for impulse noise suppression	52
4.8	Computational complexity	53
4.9	Simulation and numerical examples	54
5	Baseband Architecture	56
6	Conclusion	63
	Bibliography	63



List of Figures

1.1	The mother convolutional code of rate 1/2.	3
1.2	Puncturing pattern and transmitted sequence.	4
1.3	Inner coding and interleaving.	4
1.4	Mapping of input bits onto modulation symbols.	5
1.5	Symbol interleaver address generation scheme for the 2K mode.	6
1.6	DVB-T scatter pilot structure.	7
1.7	Carrier indices for continual pilot carriers.	7
1.8	Basic block diagram of a DVB-T system.	8
1.9	Outer interleaver and deinterleaver.	9
2.1	Structure of OFDM signal with cyclicly extended symbol $s(n)$ in non-dispersive channel.	12
2.2	MMSE synchronization. Symbol start position at the 500th sample. . . .	13
2.3	MC synchronization. Symbol start position at the 500th sample.	14
2.4	The MSE performance of coarse two timing synchronizers.	15
2.5	The MSE performance of two fractional frequency offset synchronizers. .	16
2.6	Structure of an extended OFDM frame showing the relation of the channel impulse response duration and the legitimate starting position of the FFT window.	17
2.7	The Lock-in probability of coarse timing synchronizer in AWGN and (DVB-T defined) Rayleigh fading channels.	18
2.8	Block diagram of the LS coarse timing synchronization algorithm.	19

2.9	Block diagram of a coarse frequency synchronization algorithm.	20
2.10	Frequency domain correlation when the true carrier frequency offset is $2/T$	21
2.11	Compensation characteristic of coarse frequency synchronizers with the carrier frequency offset ranges from 1.5 to 2.5 subcarrier spacings (6.696KHz to 11.16KHz in 2K mode of DVB-T system).	22
2.12	Determination of the thresholds used in (2.17) by examining the behavior of the averaged ratio between the peak correlation and second largest correlation, $E[c] = E\{\max(\phi_{M-1}/\phi_M, \phi_{M+1}/\phi_M)\}$, as a function of the normalized carrier frequency offset.	23
2.13	The MSE performance of the coarse frequency synchronizer where χ ranges from 1.5 to 2.5 (6.696KHz to 11.16KHz in 2K mode).	24
2.14	Learning curves of the conventional carrier frequency synchronizer.	25
2.15	Learning curves of modified fast carrier frequency synchronizer.	25
3.1	Generation of PRBS sequence.	27
3.2	A typical DVB-T channel's impulse response with a duration of 12 taps.	29
3.3	The DVB-T single frequency network (SFN) concept.	30
3.4	Combined impulse response of a DVB-T single frequency network with two stations.	31
3.5	LS channel estimation, $m \in \text{pilot}$ and $k = 0, \dots, N - 1$	32
3.6	A typical transform domain response $\hat{G}_p(p)$ when (a) AWGN and Doppler shift are absent (i.e., noiseless static channel) and (b) SNR = 5 dB, Doppler frequency = 90 Hz.	34
3.7	Block diagram of a channel estimation algorithm based on transform-domain processing; $m \in \text{pilots}$ and $k = 0, \dots, N - 1$ and $p = 0, \dots, N_p - 1$	35
3.8	Complete channel estimation process incorporating transform domain filtering; $m \in \text{pilot set}$ and $k = 0, \dots, N - 1$	35
3.9	Indication of the least-squared-fitting processing.	37

3.10	DVB-T pilot symbol distribution in time-frequency. In the button of this figure, regres.(3,4) means that use 3 pilots in time domain and 4 pilots in frequency domain to make regression model.	38
3.11	Block diagram of a two-stage channel estimator that consists of a TDP unit and a model-based channel estimation unit.	39
3.12	BER performance comparison of various channel estimates; zero Doppler shift, r.m.s. delay spread = $1.36 \mu s$	41
3.13	BER performance comparison of various channel estimates; Doppler frequency = 88 Hz, r.m.s. delay spread = $5.13 \mu s$	42
3.14	The effect of the 2D model size on the BER performance; Doppler shift = 88 Hz, r.m.s. delay spread = $9.1245 \mu s$	42
3.15	The effect of the FFT window size on the BER performance; Doppler frequency = 88 Hz, r.m.s. delay spread = $1.36 \mu s$	43
4.1	The Cook pulse (An impulse noise model).	45
4.2	Impulse noise and blanking noise	47
4.3	Modeling Impulse noise as clipping noise.	48
4.4	Decision-aided reconstruction for impulse noise suppression (DARINS) operation flow.	49
4.5	Initial channel estimation for DARINS (a) FSA (b) OSA.	50
4.6	The operation flow of propose algorithm. (DARINS with ICE).	52
4.7	QPSK modulation, code rate is $\frac{1}{2}$ in DVB-T Rayleigh fading channel with impulse noise (Cook pulse). Iteration 3 times. regres. (3,3). Doppler frequency $0 Hz$. r.m.s. delay spread $1.36 \mu s$ (12.5 OFDM sample).	55
4.8	QPSK modulation, code rate is $\frac{1}{2}$ in DVB-T Rayleigh fading channel with impulse noise (Cook pulse). Doppler frequency from $44 Hz$. r.m.s. delay spread $5.13 \mu s$ (48 OFDM sample).	55

5.1	Proposed DVB-T baseband receiver architecture.	59
5.2	The architecture of the coarse timing and fine frequency offset synchronization unit.	60
5.3	The architecture of the coarse frequency offset synchronization unit.	60
5.4	The architecture of the 2D model-based channel estimator with transform-domain processing.	61
5.5	Architecture of the timing tracking unit.	61
5.6	Block diagram showing the architecture for the DARINS with ICE algorithm.	62
5.7	An estimation of the overall system execution time, symbol 0 to symbol 2 is in the regular mode while symbol 9 to 10 is in the IN (impulse noise) mode.	62



List of Tables

3.1 Path gains and phase rotations associated with the DVB-T channel im- pulse response of Fig. 3.2.	32
---	----



Chapter 1

Introduction

A wideband communication channel is usually characterized by both time-selective and frequency-selective fading. The Orthogonal frequency division modulation (OFDM) technique converts a wideband signal into an array of narrowband signals for parallel transmission so that each narrow band signal suffers from frequency-nonsselective fading. If the symbol time is less than the coherent time and a cyclic prefix longer than the maximum delay of the channel is inserted in every symbol, the receiver needs only a one-tap equalizer to compensate for the corresponding complex multiplicative channel distortion.

Because of its anti-fading capability and high spectral efficiency and, equally importantly, since the corresponding hardware realization technology has become feasible and affordable, OFDM has arisen intensive interest in the worldwide telecommunication community in the past decade and has been adopted as the radio transmission technique for European digital video terrestrial broadcasting (DVB-T) standard [1] and wireless local area network (LAN) standards like IEEE 802.11a and 802.11g physical layer (PHY) [2].

DVB-T, the Terrestrial Digital TV system, is now widely deployed around the world, using its more natural modes to deliver a maximum of programmes to fix, portable and even mobile receivers. The spectrum and economical efficiencies of the DVB-T standard are derived from its hierarchical modulation modes which offer a way to deploy two

independent services using only one radio frequency channel and only one transmitter. As will be shown in Chapter 3, the Single Frequency Networks (SFN) mode of operation further improves the spectrum efficiency of DVB-T.

Two major synchronization issues arise in the design of an OFDM receiver. The first one is the detection and estimation of the OFDM symbol arrival time. Sensitivity to a time offset is higher in multicarrier systems than in single-carrier systems. The second issue of concern has to do with the frequency offset. Frequency offset is due both to the Doppler effect in the mobile communication environments and to the instabilities of and mismatch between the transmitter and the receiver oscillators. The demodulation of an OFDM signal with a nonzero frequency offset cause inter-carrier interference (ICI) and results in higher bit error rates. ICI also affects the performance of other synchronization subsystems and might incur inter-symbol interference (ISI) that is supposed to be eliminated by inserting guard intervals between successive OFDM symbols.

A radio communication system may experience several kinds of impairments. The combination of thermal, atmospheric, or galactic noise can be represented by a stationary Gaussian random processes. However, man-made noise that appears in urban environments created by the electrical self-starter of cars, power lines, heavy current switches, arc welders, fluorescent lights, etc., cannot be assumed to be Gaussian nor are they stationary. As it has a relatively short duration, it is more appropriately represented by an impulse noise (IN) model. Besides presenting synchronization, channel estimation and IN suppression (INS) algorithms, the other main theme of this thesis is to propose a baseband architecture that can operate in a normal mode when no impulse noise is present and is capable of switching to the impulse-noise-suppression (INS) mode automatically when impulse noise is present.

The rest of this thesis is organized as follows. The ensuing section introduces the basic DVB-T system structure. Chapter 2 then presents algorithms for timing and frequency synchronization. An effective channel estimator is proposed in Chapter 3. In Chapter

4, we present an algorithm for impulse noise suppression and its extended version that perform both INS and channel estimation. Chapter 5 outlines a baseband architecture and finally, Chapter 6 summarizes our main contributions and draws concluding remarks.

1.1 DVB-T systems

Fig. 1.8 illustrates the European standard (ETSI) of terrestrial system for digital video broadcasting (DVB-T) whose specifications are described in the followings. The source bits unit transmits data stream in the format of MPEG-2 transport layer defined by the ISO/IEC 13818-1 standard. The outer code is the shortened $(204,188,t=8)$ Reed-Solomon (RS) code that derived from the original systematic $(255, 239, t = 8)$ RS code. Fig. 1.9 illustrates the convolutional byte-wise (outer) interleaver with depth $I = 12$ that is applied to the RS-encoded packet. The outer-interleaved bytes, after a byte-to-bit conversion, are then send to the convolutional inner encoder. The system allows for a range of punctured convolutional codes, based on a mother convolutional code of rate $1/2$ with 64 states; see Fig. 1.1.

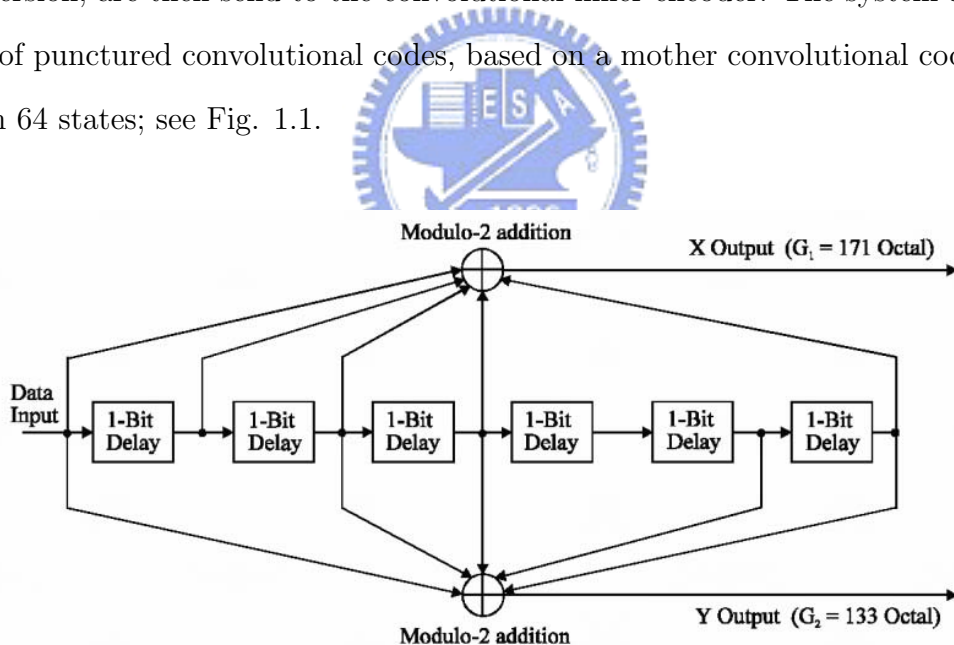


Figure 1.1: The mother convolutional code of rate $1/2$.

The puncture patterns are given in Fig. 1.2 where the labels X and Y refer to the two convolutional encoder outputs that are further permuted by the inner interleaver

shown in Fig. 1.3.

Code Rates r	Puncturing pattern	Transmitted sequence (after parallel-to-serial conversion)
1/2	X: 1 Y: 1	$X_1 Y_1$
2/3	X: 1 0 Y: 1 1	$X_1 Y_1 Y_2$
3/4	X: 1 0 1 Y: 1 1 0	$X_1 Y_1 Y_2 X_3$
5/6	X: 1 0 1 0 1 Y: 1 1 0 1 0	$X_1 Y_1 Y_2 X_3 Y_4 X_5$
7/8	X: 1 0 0 0 1 0 1 Y: 1 1 1 1 0 1 0	$X_1 Y_1 Y_2 Y_3 Y_4 X_5 Y_6 X_7$

Figure 1.2: Puncturing pattern and transmitted sequence.

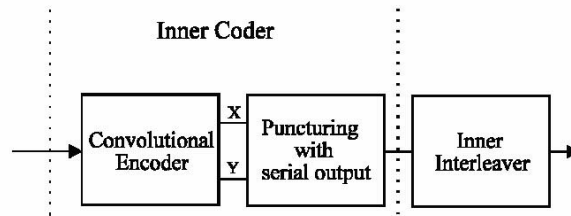


Figure 1.3: Inner coding and interleaving.

The inner interleaving consists of bit-wise interleaving (Fig. 1.4) followed by symbol interleaving (Fig. 1.5). Both bit-wise interleaving and the symbol interleaving processes are block-based.

As mentioned before, the system uses OFDM transmission. All data carriers in one OFDM frame are modulated by either QPSK, 16-QAM, 64-QAM, non-uniform 16-QAM or non-uniform 64-QAM constellations. The exact values of the constellation point are $z \in \{u + jv\}$ with values of u, v given below for the various constellations:

QPSK

$$u \in -1, 1, v \in -1, 1$$

16-QAM

$$u \in -3, -1, 1, 3, v \in -3, -1, 1, 3$$

Non-uniform 16-QAM

$$u \in -4, -1, 1, 4, v \in -4, -1, 1, 4$$

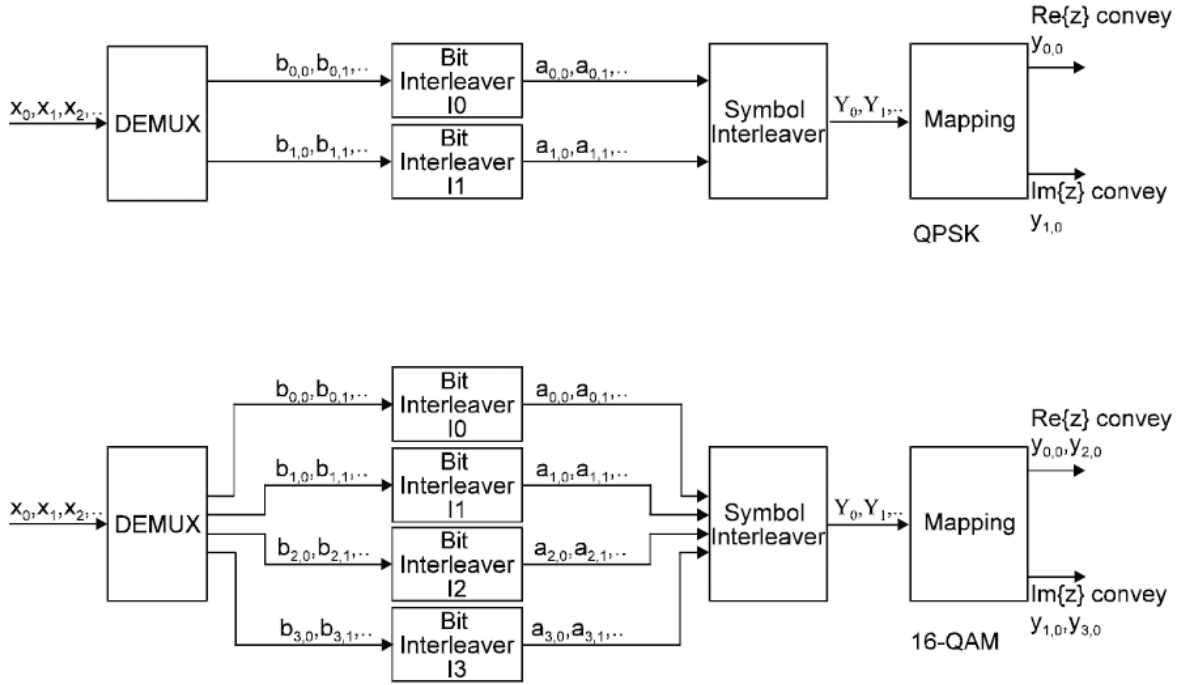


Figure 1.4: Mapping of input bits onto modulation symbols.

64-QAM

$$u \in -7, -5, -3, -1, 1, 3, 5, 7, v \in -7, -5, -3, -1, 1, 3, 5, 7$$

Non-uniform 64-QAM

$$u \in -8, -6, -4, -2, 2, 4, 6, 8, v \in -8, -6, -4, -2, 2, 4, 6, 8.$$

The transmitted signal is organized in frames. Each frame has a duration of T_F and consists of 68 OFDM symbols. Four frames form a super-frame. Each symbol is constituted by a set of $K = 6817$ carriers in $8K$ mode and $K = 1705$ carriers in $2K$ mode and is transmitted with a duration of T_S . It is composed two parts: a useful (information) part with duration T_U and a guard interval (cyclic prefix) with duration Δ . The symbols in an OFDM frame are numbered from 0 to 67. All symbols contain data and reference information. In addition to the transmitted data an OFDM frame contains scatter pilot, continual pilot and TPS (transmission parameter signalling) carriers. Location of scatter pilot is shown in Fig. 1.6. There are 177 continual pilots in the $8K$ mode and

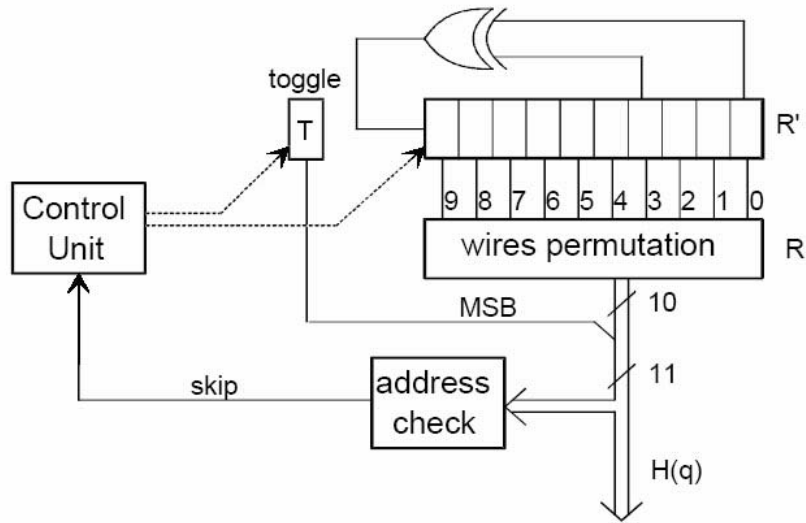


Figure 1.5: Symbol interleaver address generation scheme for the 2K mode.

45 in 2K mode; they are inserted according to Fig. 1.7. The TPS carriers are used for the purpose of signalling parameters related to the transmission scheme that includes channel coding and modulation. The TPS is transmitted in parallel on 17 TPS carriers for 2K mode and on 68 carriers for the 8K mode.

For the receiver performs reverse operations of transmitter properly, it needs a synchronizer to supply correct estimates for extracting the timing, carrier and frequency offset information and an channel equalizer to compensate for the frequency domain distortion incurred by the transmission channel. The following chapter presents some feasible solutions to the synchronization subsystem design.

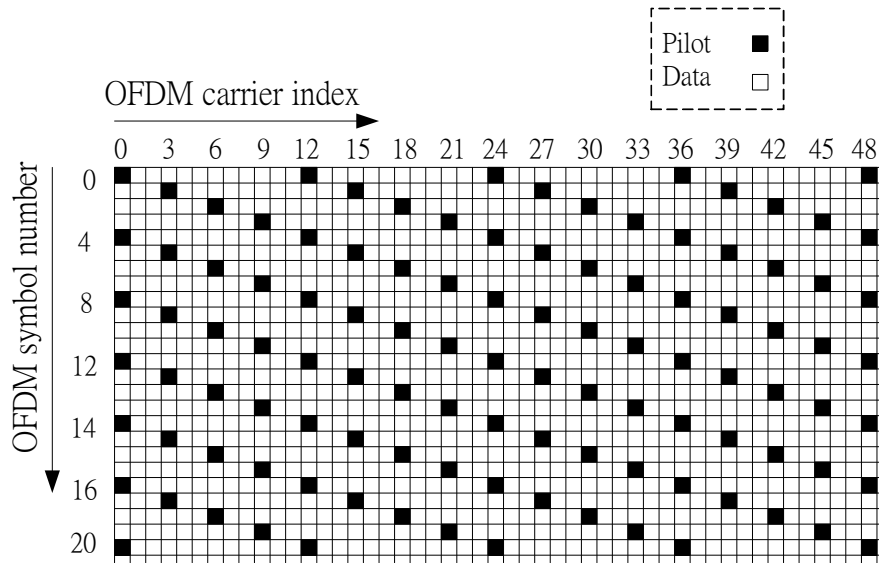


Figure 1.6: DVB-T scatter pilot structure.



Continual pilot carrier positions (index number k)	
2K mode	8K mode
0 48 54 87 141 156 192 201 255 279 282 333 432 450	0 48 54 87 141 156 192 201 255 279 282 333 432 450
483 525 531 618 636 714 759 765 780 804 873 888 918	483 525 531 618 636 714 759 765 780 804 873 888
939 942 969 984 1050 1101 1107 1110 1137 1140 1146	918 939 942 969 984 1050 1101 1107 1110 1137 1140
1206 1269 1323 1377 1491 1683 1704	1146 1206 1269 1323 1377 1491 1683 1704 1752 1758
	1791 1845 1860 1896 1905 1959 1983 1986 2037 2136
	2154 2187 2229 2235 2322 2340 2418 2463 2469 2484
	2508 2577 2592 2622 2643 2646 2673 2688 2754 2805
	2811 2814 2841 2844 2850 2910 2973 3027 3081 3195
	3387 3408 3456 3462 3495 3549 3564 3600 3609 3663
	3687 3690 3741 3840 3858 3891 3933 3939 4026 4044
	4122 4167 4173 4188 4212 4281 4296 4326 4347 4350
	4377 4392 4458 4509 4515 4518 4545 4548 4554 4614
	4677 4731 4785 4899 5091 5112 5160 5166 5199 5253
	5268 5304 5313 5367 5391 5394 5445 5544 5562 5595
	5637 5643 5730 5748 5826 5871 5877 5892 5916 5985
	6000 6030 6051 6054 6081 6096 6162 6213 6219 6222
	6249 6252 6258 6318 6381 6435 6489 6603 6795 6816

Figure 1.7: Carrier indices for continual pilot carriers.

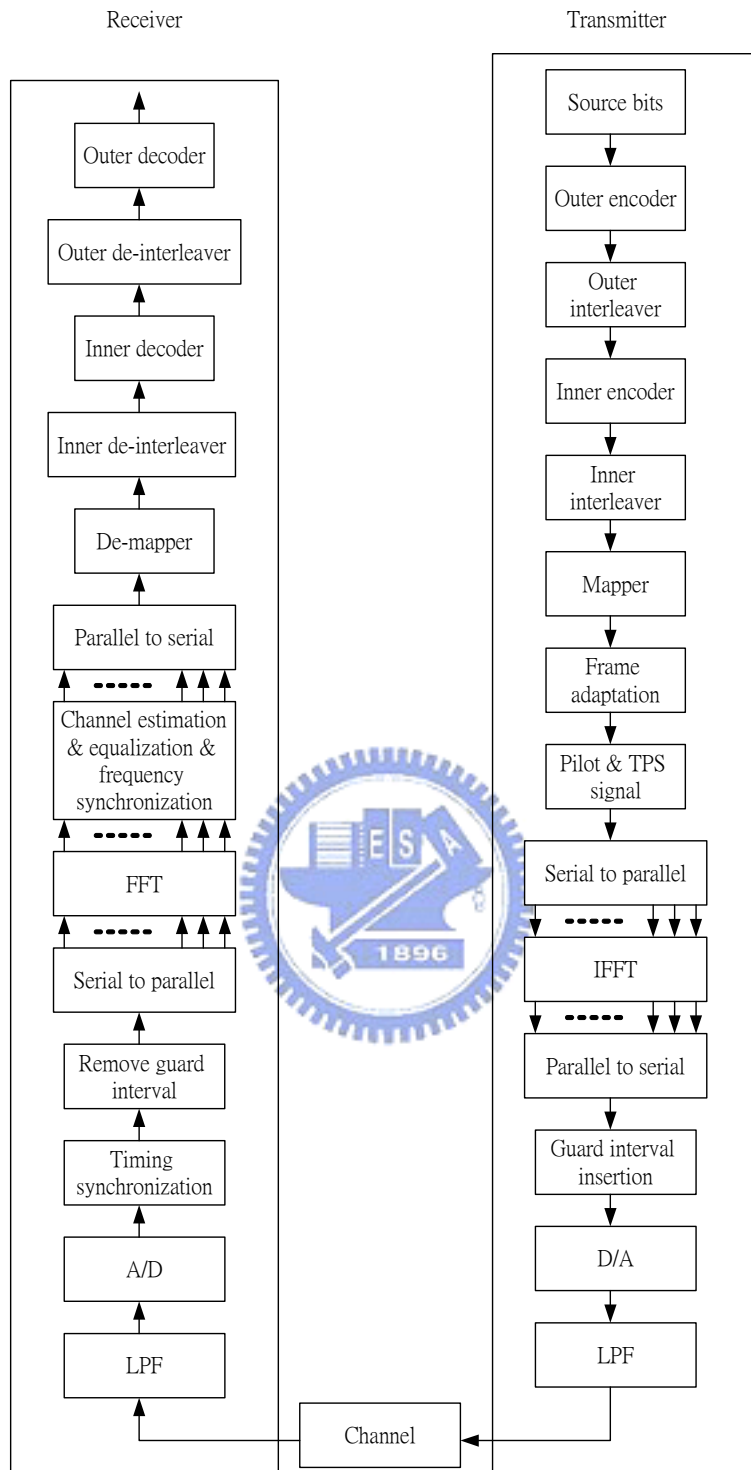


Figure 1.8: Basic block diagram of a DVB-T system.

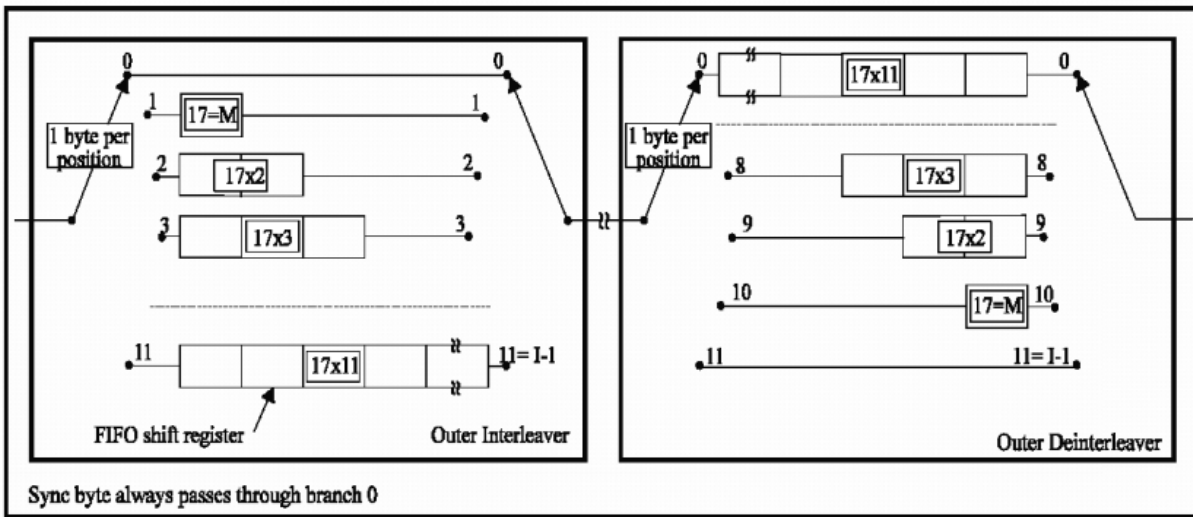


Figure 1.9: Outer interleaver and deinterleaver.

Chapter 2

Frequency and Timing Synchronization Subsystems

Synchronization is an essential part for any digital communication system. Without accurate synchronization, it is impossible to reliably recover the transmitted data. In this chapter we address both timing and frequency synchronization issues associated with a DVB-T receiver.

2.1 Joint coarse timing and fractional frequency offset estimation



The estimation of the symbol starting position determines the alignment of the fast Fourier transform (FFT) window in the receiver with the useful portion of the desired OFDM symbol. A false estimate leads to inter symbol interference (ISI) and is likely to destroy the orthogonality of the received signal and the resulting inter channel interference (ICI) causes severe performance degradation. Timing estimation consists of two main tasks—signal (presence) detection and symbol synchronization. In a broadcast system, however, a receiver does not need to detect the presence of a transmitted waveform, because it is always there. Although in deriving our synchronizer we assume that the channel is non-dispersive and the only perturbation source is additive white Gaussian noise (AWGN) $w(n)$, our simulation indicates that the algorithm works for both AWGN and time dispersive channels.

The time-frequency uncertainty in the received OFDM waveform consists of the uncertainty about the signal arrival time and that about the carrier frequency. The time uncertainty manifests itself in the delay associated with the channel impulse response $\delta(n - \theta)$, where θ is assumed to be a multiple of the sampling interval. The frequency uncertainty results in an additional multiplicative term $e^{j2\pi\chi n/N}$ on the received signal, where $\chi = \Omega + \varepsilon = \Delta f/T$, Δf being the frequency offset in Hz, T the OFDM frame interval, Ω an integer, and $0 \leq \varepsilon < 1$. Hence χ denotes the normalized frequency offset as a multiple of the subcarrier space $1/T$, Ω is the integer part of ζ while ε is the fractional part. The frequency synchronization process is often divided into two stage, one for compensating for the integer part, Ω , and is referred to as coarse synchronization, and the other is responsible for estimating the fractional part ε . It is assumed that all subcarriers experience the same frequency shift ζ . When dealing with estimating the fractional part only, we can, without loss of generality, assume that

$$r(n) = s(n - \theta)e^{j2\pi\varepsilon n/N} + w(n), \quad 0 < \varepsilon < 1. \quad (2.1)$$

In what follows, we show that both the frequency and time synchronization can be derived from the received signal samples' cyclic prefix. Several coarse symbol synchronization algorithms utilizing the cyclic prefix have been investigated for OFDM systems adopting the maximum correlation (MC) [4], or the minimum mean-squared error (MMSE) [5] criterion.

Suppose, as shown in Fig. 2.1, we have collected $2N + N_g$ consecutive samples of $r(n)$ during the observation interval and the samples contain $(N + N_g)$ consecutive samples associated with one complete OFDM symbol. Because the channel delay θ is not known, we have find out which sample represents the starting position of that complete symbol. Define the index sets

$$\zeta \equiv \{\theta, \dots, \theta + N_g - 1\} \quad (2.2)$$

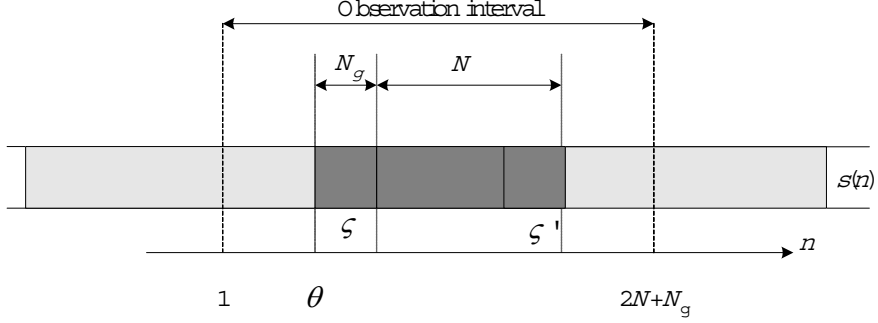


Figure 2.1: Structure of OFDM signal with cyclicly extended symbol $s(n)$ in non-dispersive channel.

and

$$\zeta' \equiv \{\theta + N, \dots, \theta + N + N_g - 1\} \quad (2.3)$$

and denote the $(2N + N_g)$ samples by the vector $\mathbf{r} = [r(1) \cdots r(2N + N_g)]^T$. As the cyclic prefix is copied from $\{r(n), n \in \zeta'\} = \mathbf{r}_{\zeta'}$, both are highly correlated while the remaining samples $\{r(n), n \notin \zeta \cup \zeta'\}$ are independent from them. Many algorithms have exploited this property for timing offset estimation. Speth, Classen, and Meyr [5] suggested that by minimizing the metric

$$\Lambda(\theta) = \sum_{n=0}^{N_g-1} |r(\theta + n + N) - r(\theta + n)|^2 \quad (2.4)$$

where N is the FFT window size, one can jointly estimate the coarse symbol start position and the frequency offset by the following algorithm

$$\begin{aligned} \hat{\theta}_{MMSE} &= \arg \min_{\theta} \{\Phi(\theta) - |\gamma(\theta)|\} = \arg \max_{\theta} \{|\gamma(\theta)| - \Phi(\theta)\} \\ \hat{\epsilon}_{MMSE} &= -\frac{1}{2\pi} \angle \gamma(\hat{\theta}_{MMSE}) \end{aligned} \quad (2.5)$$

where

$$\begin{aligned} \gamma(\theta) &= \sum_{n=\theta}^{\theta+N_g-1} r(n)r^*(n+N), \\ \Phi(\theta) &= \frac{1}{2} \sum_{n=\theta}^{\theta+N_g-1} (|r(n)|^2 + |r(n+N)|^2) \end{aligned} \quad (2.6)$$

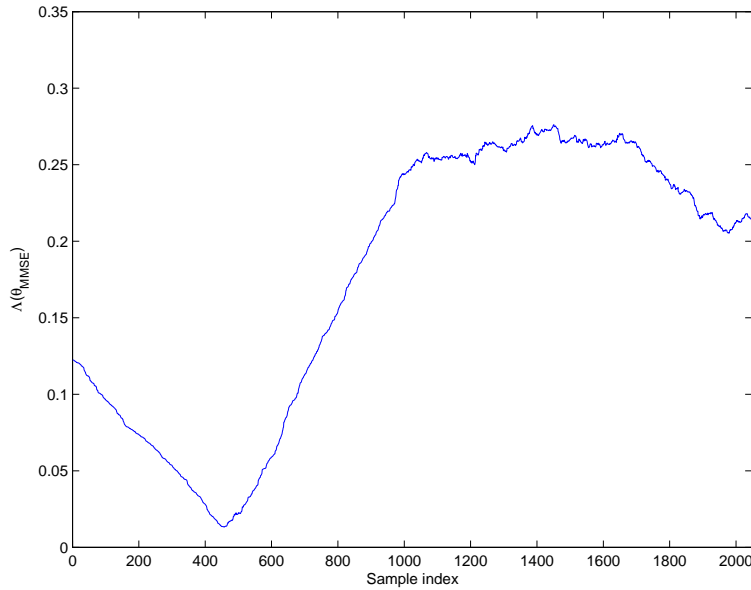


Figure 2.2: MMSE synchronization. Symbol start position at the 500th sample.

The term $\Phi(\theta)$ is an energy term, its contribution depends on the $\text{SNR} = \sigma_s^2/\sigma_n^2$; furthermore, the magnitude of the correlation coefficient between $r(n)$ and $r(n + N)$ is given by

$$\rho = \left| \frac{E\{r(n)r^*(n + N)\}}{\sqrt{E\{|r(n)|^2\}E\{|r(n + N)|^2\}}} \right| = \frac{\sigma_s^2}{\sigma_s^2 + \sigma_n^2} = \frac{\text{SNR}}{\text{SNR} + 1}. \quad (2.7)$$

Keller and Hanzo proposed the MC algorithm [4], which is perhaps the simplest joint timing and frequency offset estimate

$$\hat{\theta}_{MC} = \arg \max_{\theta} \{|\gamma(\theta)|\} \quad (2.8)$$

$$\hat{\varepsilon}_{MC} = -\frac{1}{2\pi} \angle \gamma(\hat{\theta}_{MC}). \quad (2.9)$$

Obviously, the complexity of MMSE algorithm is higher than that of the MC algorithm whilst its performance is improved with the increasing complexity. Fig. 2.4 plots the MSE performance of coarse timing estimate and Fig. 2.5 plots the MSE performance of fractional frequency offset tracking.

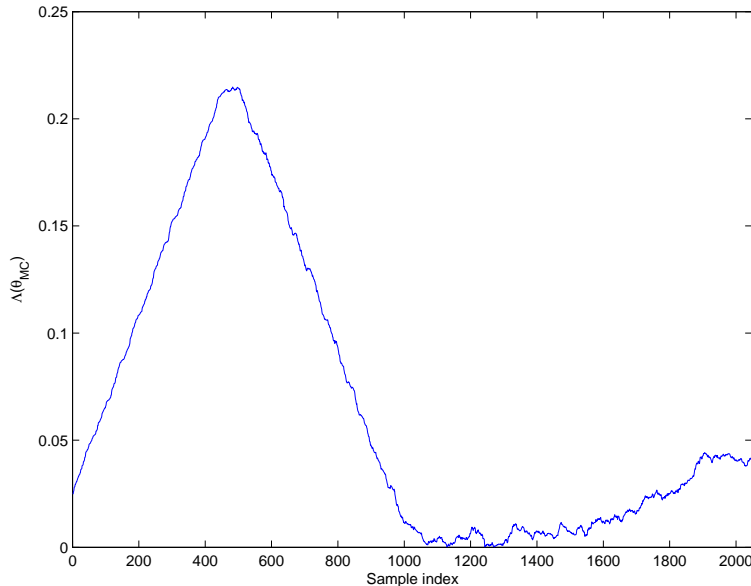


Figure 2.3: MC synchronization. Symbol start position at the 500th sample.

2.1.1 Coarse timing recovery in multipath fading channels

The above coarse timing synchronization algorithms are derived under the assumption that the only noise source is AWGN. They yield satisfactory performance in a multipath channel in which the leading arrival path is the strongest. If this is not the case, as shown in Fig.2.6 where the presence of multipath propagation makes a part of the guard interval be interfered by the preceding symbol, these algorithms are likely to give wrong timing estimation and will result in ISI. No ISI occurs if the starting position of the FFT window is within region *A*. The only effect on the subcarriers is a phase rotation that increases with the subcarrier index. On the other hand, if the starting position of the FFT window is within region *B*, the subcarriers will suffer from ISI in addition to the phase rotation, and the orthogonality amongst subcarriers is destroyed. The received signal can then be expressed as

$$r(n) = (s(n) \otimes h(n))e^{j2\pi\epsilon n/N} + w(n). \quad (2.10)$$

where $h(n)$ is the impulse response of channel and $w(n)$ is the AWGN. Lee and Cheun (LS) [3] modified the MMSE and MC synchronization algorithms mentioned before to

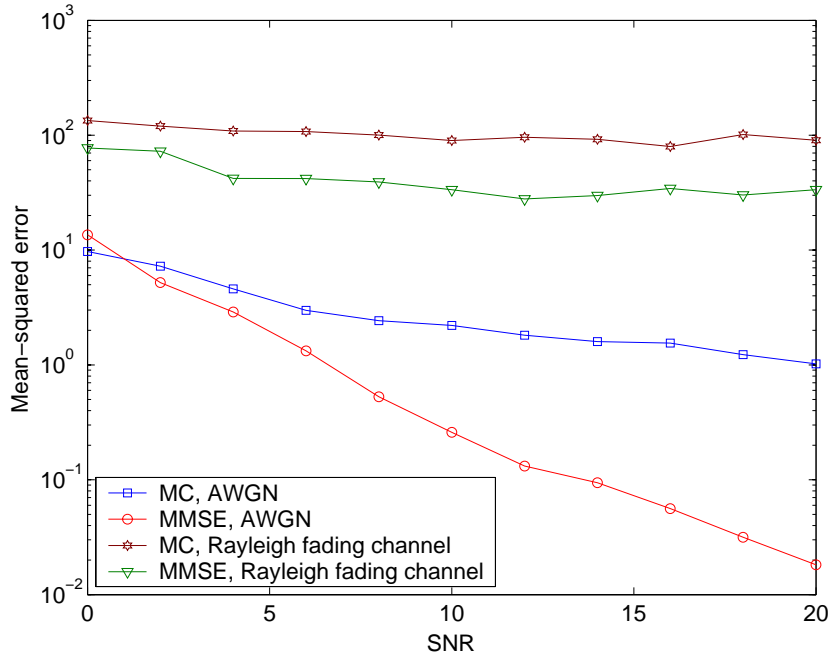


Figure 2.4: The MSE performance of coarse two timing synchronizers.

design coarse timing synchronization algorithms for OFDM systems in multipath channels in which the leading path is not the strongest one. The modification made in [3] is simple and straightforward, it only uses an extended sample interval. The LS algorithm extends the sample interval used by $\Phi(\theta)$ and $\gamma(\theta)$ from $[\theta, (\theta + N_g - 1)]$ to $[\theta, (\theta + N_{s1} - 1)]$ or $[\theta, (\theta + N_{s2} - 1)]$, where $N_{s1} = N_g + N_m$ and $N_{s2} = 2N_g - 1$, N_m being maximum delay spread. Hence $\Phi(\theta)$ and $\gamma(\theta)$ are modified according to

$$\gamma(\theta) = \sum_{n=\theta}^{\theta+N_{s1}-1} r(n)r^*(n+N) \quad \text{or} \quad \gamma(\theta) = \sum_{n=\theta}^{\theta+N_{s2}-1} r(n)r^*(n+N), \quad (2.11)$$

$$\Phi(\theta) = \frac{1}{2} \sum_{n=\theta}^{\theta+N_{s1}-1} |r(n)|^2 + |r(n+N)|^2 \quad \text{or} \quad \Phi(\theta) = \frac{1}{2} \sum_{n=\theta}^{\theta+N_{s2}-1} |r(n)|^2 + |r(n+N)|^2 \quad (2.12)$$

A block diagram of this modified coarse timing synchronizer is given in Fig. 2.8.

2.2 Coarse frequency synchronization

Coarse frequency synchronization refers to the estimation of the integer part Ω of the frequency uncertainty. One of the most popular coarse frequency synchronization al-

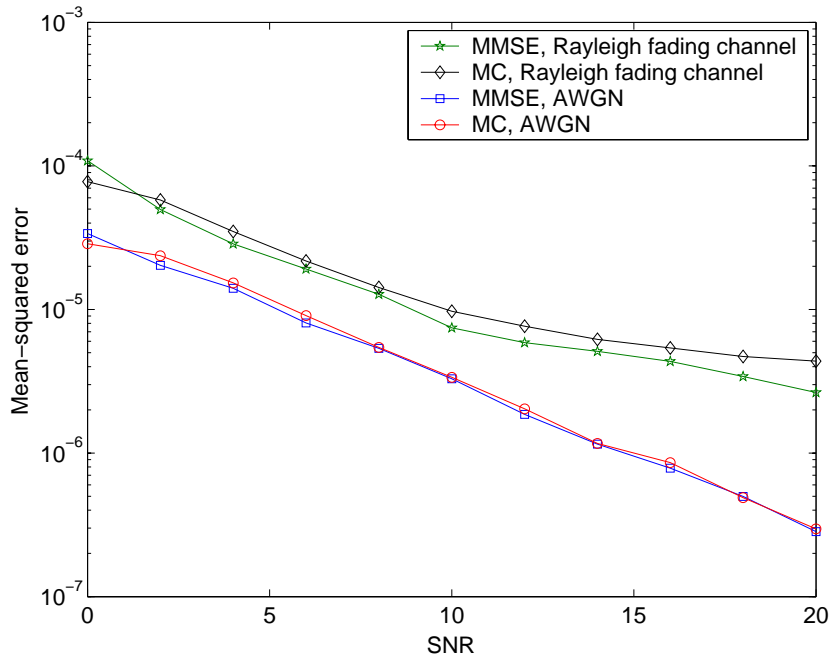


Figure 2.5: The MSE performance of two fractional frequency offset synchronizers.

gorithms for OFDM signals is to detect the location of guard bands (virtual carriers) which are supposed to be located at both edges of the OFDM spectrum to avoid adjacent channel interference. We can use this algorithm to estimate coarse frequency offset of a DVB-T signal. Han [7] proposed a two-stage frequency domain algorithm for coarse frequency synchronization. As shown in Fig. 2.9, it first calculates the correlation of two frequency domain pilots associated with the same subcarrier for two successive symbols at candidate frequency-shifted pilot positions. In other words, if $R_i(k)$ represents the i th symbol of the k th subcarrier, $P_m = [p_1 + m, p_2 + m, \dots, p_L + m]$ is the set of the subcarriers to be correlated and m denotes the subcarrier offset from P_0 , then the coarse frequency estimate is given by

$$\hat{\Omega}_o = \arg \max_m (\phi_m), \quad \text{where } \phi_m = \left| \sum_{k \in P_m} R_i(k) R_{i+1}^*(k) \right|. \quad (2.13)$$

Fig. 2.10 illustrates the correlation process when the received frequency domain signal has a normalized carrier frequency offset of two. We use the continual pilots for coarse frequency synchronization in our DVB-T system, the positions of the continual pilot [1]

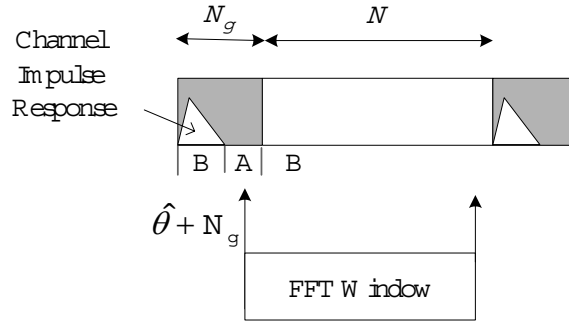


Figure 2.6: Structure of an extended OFDM frame showing the relation of the channel impulse response duration and the legitimate starting position of the FFT window.

indices are $0, 48, 54, 87, \dots$. If the maximum value ϕ_M is obtained from correlating with subcarriers $2, 50, 56, 89, \dots$, the estimated integer frequency offset is two because the position of the maximum correlation is obtained at two subcarrier spacings away from the original continual pilots. The second stage is needed to improve the performance of the first stage when the fractional carrier offset is around $+0.5$ or -0.5 . We then use the ratio of the maximum value ϕ_M and one of its adjacent values ϕ_{M+1} or ϕ_{M-1} to reduce the carrier frequency uncertainty.

$$\hat{\Omega} = \begin{cases} \hat{\Omega}_o - 0.5, & \text{if } \phi_{M-1} > \phi_{M+1} \text{ and } \frac{\phi_{M-1}}{\phi_M} > \mu_1, \\ \hat{\Omega}_o + 0.5, & \text{if } \phi_{M-1} < \phi_{M+1} \text{ and } \frac{\phi_{M+1}}{\phi_M} > \mu_2 \\ \hat{\Omega}_o, & \text{elsewhere,} \end{cases} \quad (2.14)$$

where μ is a pre-determined threshold.

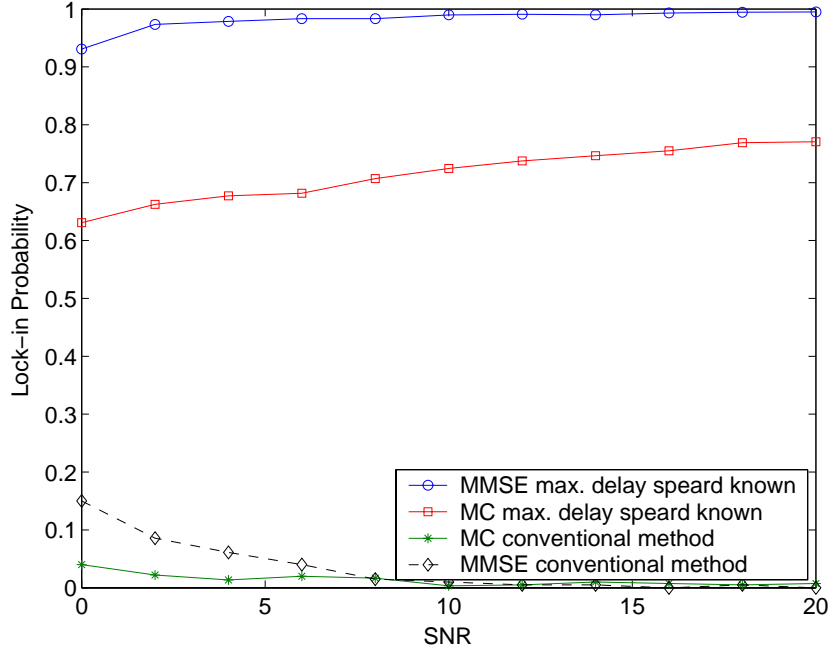


Figure 2.7: The Lock-in probability of coarse timing synchronizer in AWGN and (DVB-T defined) Rayleigh fading channels.

2.2.1 Improved coarse frequency synchronization

Based on Han's idea, we propose the following extended version of (2.14) for fine frequency synchronization

$$\hat{\chi} = \begin{cases} \hat{\Omega}_o - 0.1, & \text{if } \phi_{M-1} > \phi_{M+1} \text{ and } \frac{\phi_{M-1}}{\phi_M} > \mu_{-1}, \\ \hat{\Omega}_o - 0.2, & \text{if } \phi_{M-1} > \phi_{M+1} \text{ and } \frac{\phi_{M-1}}{\phi_M} > \mu_{-2}, \\ \hat{\Omega}_o - 0.3, & \text{if } \phi_{M-1} > \phi_{M+1} \text{ and } \frac{\phi_{M-1}}{\phi_M} > \mu_{-3}, \\ \hat{\Omega}_o - 0.4, & \text{if } \phi_{M-1} > \phi_{M+1} \text{ and } \frac{\phi_{M-1}}{\phi_M} > \mu_{-4}, \\ \hat{\Omega}_o - 0.5, & \text{if } \phi_{M-1} > \phi_{M+1} \text{ and } \frac{\phi_{M-1}}{\phi_M} > \mu_{-5}, \\ \hat{\Omega}_o + 0.1, & \text{if } \phi_{M-1} < \phi_{M+1} \text{ and } \frac{\phi_{M+1}}{\phi_M} > \mu_{+1} \\ \hat{\Omega}_o + 0.2, & \text{if } \phi_{M-1} < \phi_{M+1} \text{ and } \frac{\phi_{M+1}}{\phi_M} > \mu_{+2} \\ \hat{\Omega}_o + 0.3, & \text{if } \phi_{M-1} < \phi_{M+1} \text{ and } \frac{\phi_{M+1}}{\phi_M} > \mu_{+3} \\ \hat{\Omega}_o + 0.4, & \text{if } \phi_{M-1} < \phi_{M+1} \text{ and } \frac{\phi_{M+1}}{\phi_M} > \mu_{+4} \\ \hat{\Omega}_o + 0.5, & \text{if } \phi_{M-1} < \phi_{M+1} \text{ and } \frac{\phi_{M+1}}{\phi_M} > \mu_{+5} \\ \hat{\Omega}_o, & \text{elsewhere,} \end{cases} \quad (2.15)$$

where $\mu_{-5} \sim \mu_{+5}$ are thresholds to be optimized.

We add eight constraints to enhance the resolution of the coarse frequency synchro-

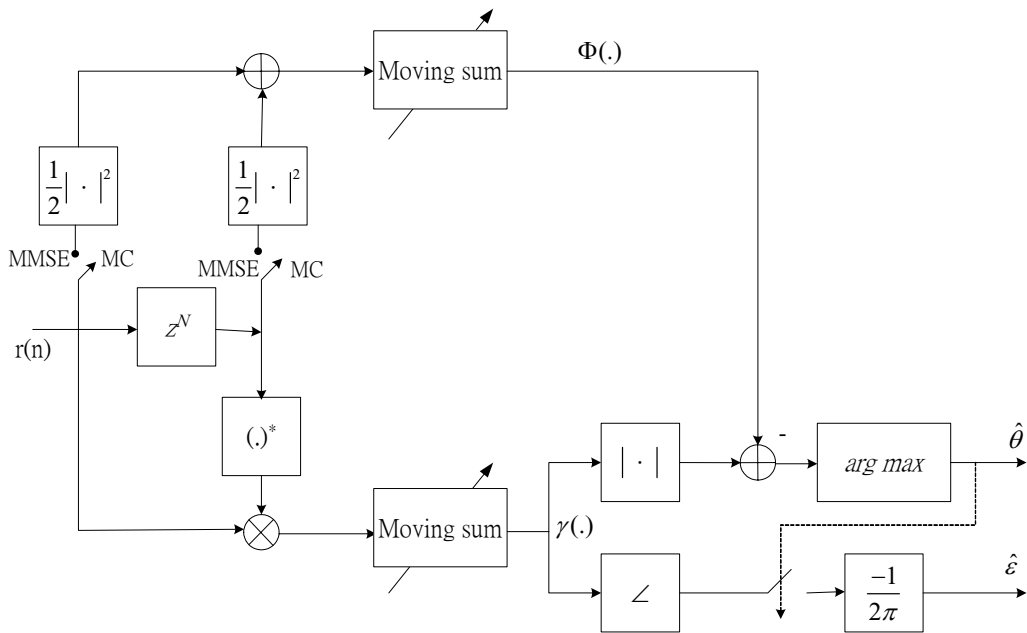


Figure 2.8: Block diagram of the LS coarse timing synchronization algorithm.

nizer from ± 0.25 to ± 0.1 . With such an enhanced resolution, the residual frequency error can easily be compensated for by any correlation-based fine frequency synchronizer and the acquisition time can be reduced significantly.

2.3 Timing tracking

After establishing the coarse frame timing, one still has to fine-tune the timing clock to improve the performance when the receiver is operating in a mobile environment. This is because the drifting of the clock will make the system lose lock and its performance deteriorate as ISI arises if the clock is left without tracking. Furthermore, a residual timing error also induces phase rotations after de-multiplexing in the frequency domain. The residual timing error is often corrected after channel equalization has been accomplished. The channel estimation/equalization procedure is presented in Chapter 3. For the moment, let us assume that the channel impulse response is perfectly known

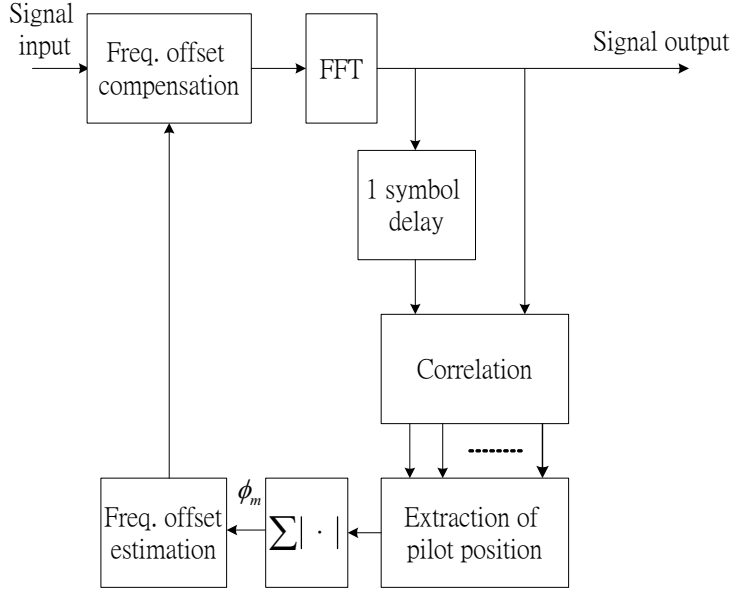


Figure 2.9: Block diagram of a coarse frequency synchronization algorithm.

and denote the frequency domain samples with perfect timing recovery by

$$R(k; 0) = \sum_{n=0}^{N-1} x(n) e^{-j2\pi kn/N} + W(k), \quad k = 0, \dots, N-1, \quad (2.16)$$

so that that corresponding to a timing error of θ_e is given by

$$\begin{aligned} R(k; \theta_e) &= \sum_{n=0}^{N-1} x(n - \theta_e) e^{-j2\pi kn/N} + W(k) \\ &= R(k; 0) e^{-j2\pi k\theta_e/N}, \quad k = 0, \dots, N-1 \end{aligned} \quad (2.17)$$

where θ_e is the residual timing error and $x(n) = s(n) \otimes h(n)$, \otimes being the convolution operation. The estimated channel responses at pilot carriers when a group delay in time domain is present can be represented by

$$\hat{H}_p(m) = H_p(m) \cdot e^{-jm\theta_e} + \Delta H_p(m), \quad m \in \text{pilot tones} \quad (2.18)$$

where $H_p(m)$ is true channel transfer function and $\Delta H_p(m)$ is the estimation error. We notice that to estimate the timing error θ_e is equivalent to estimating the unknown frequency in the sequence $\{\hat{H}_p(m)\}$. Any standard single frequency estimator, e.g., those

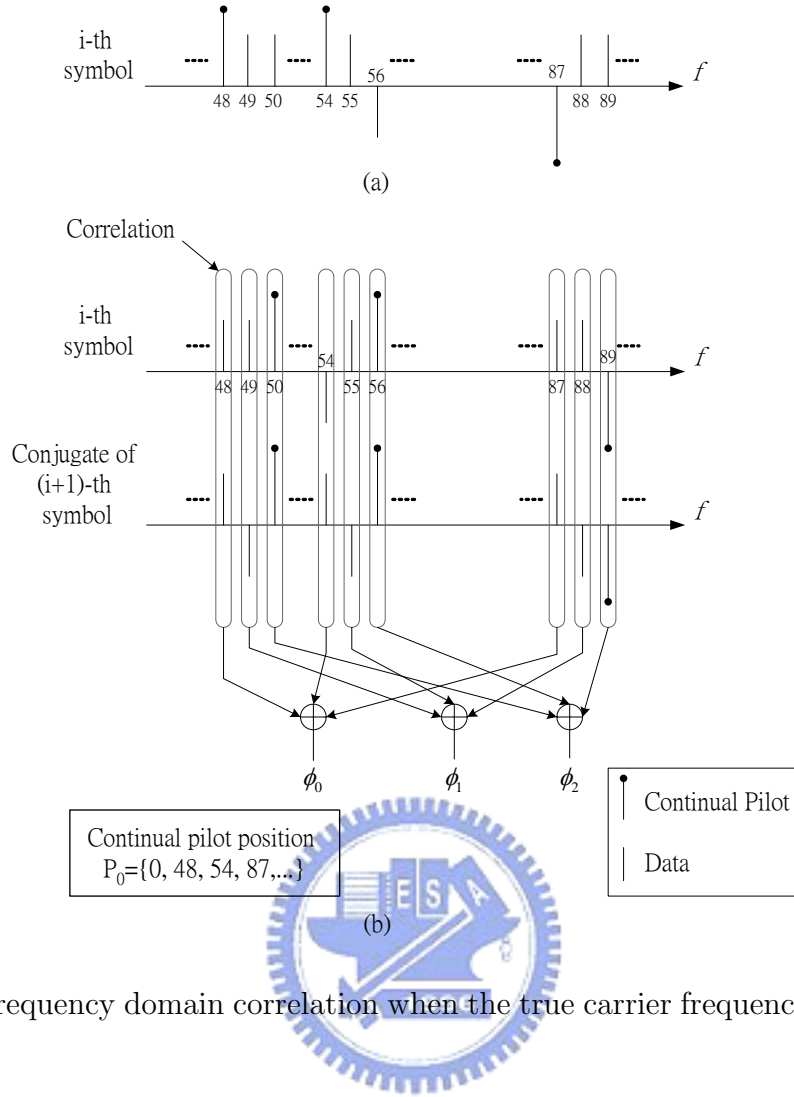


Figure 2.10: Frequency domain correlation when the true carrier frequency offset is $2/T$.

presented in [8] can be applied to estimate θ_e . The estimator in [8] that provides the best overall performance is given by

$$\hat{\theta}_e = \sum_{m=0}^{N_p-2} w(m) \angle \hat{H}_p^*(m) \hat{H}_p(m+1) \quad (2.19)$$

where N_p is the number of pilot subcarriers and

$$w_m = \frac{\frac{3}{2}N_p}{N_p^2 - 1} \left\{ 1 - \left[\frac{m - (\frac{N_p}{2} - 1)}{\frac{N_p}{2}} \right]^2 \right\} \quad (2.20)$$

A simpler but inferior estimator is [8]e phase estimator is

$$\hat{\theta}_e = \frac{1}{N-1} \sum_{m=0}^{N_p-2} \angle \hat{H}_p^*(m) \hat{H}_p(m+1) \quad (2.21)$$

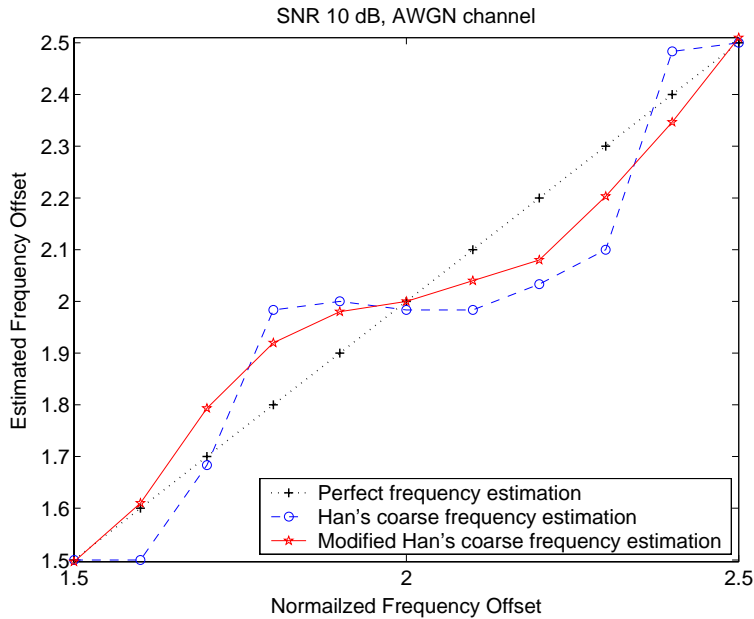


Figure 2.11: Compensation characteristic of coarse frequency synchronizers with the carrier frequency offset ranges from 1.5 to 2.5 subcarrier spacings (6.696KHz to 11.16KHz in 2K mode of DVB-T system).

2.4 Computational complexity

It has been found that between the two coarse timing synchronizers, the MMSE and MC algorithms, the former has a better performance but needs more computational complexity. The MC algorithm needs N_g additions and N_g complex multiplications while the MMSE algorithm needs extra $2N_g$ additions and $4N_g$ real multiplications. The modified coarse timing synchronizers for multipath channels necessitate even higher complexity— N_g is increased to N_{s1} or N_{s2} .

The coarse frequency offset synchronizer calls for N_{cp} additions and N_{cp} multiplications in computing ϕ_m and N -symbol memory to stored the last symbol samples, where N_{cp} is the number of continual pilot. The total complexity depends on the maximum frequency offset that we assumed. Without regard to the channel estimation, the timing tracking subsystem requires $N_p - 1$ additions and $N_p - 1$ complex multiplications when (2.21) is used.

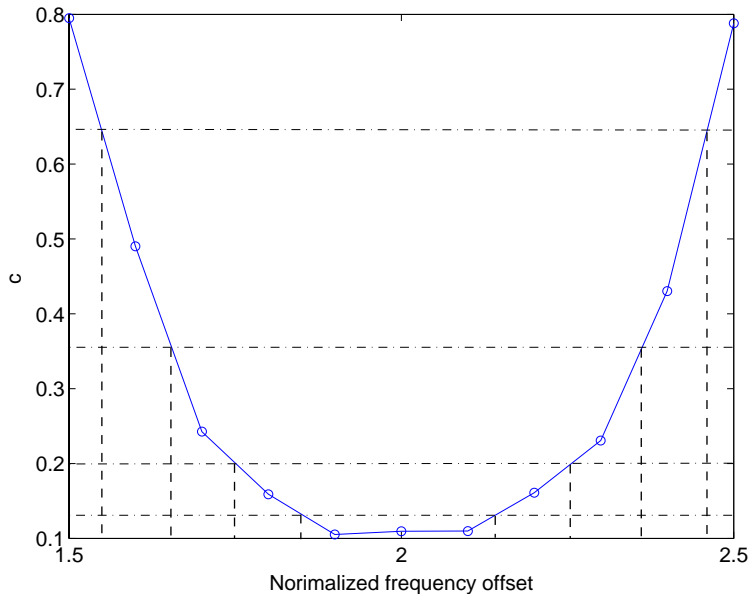


Figure 2.12: Determination of the thresholds used in (2.17) by examining the behavior of the averaged ratio between the peak correlation and second largest correlation, $E[c] = E\{\max(\phi_{M-1}/\phi_M, \phi_{M+1}/\phi_M)\}$, as a function of the normalized carrier frequency offset.

2.5 Numerical Behavior

The lock-in probability performance shown in Fig. 2.7 indicates conventional timing recovery algorithm can not overcome the multipath effect, where we have defined the lock-in probability as the probability that the FFT window starts at the legitimate region (see Fig. 2.6). One candidate solution is to extended correlation length and another one is to modify our coarse timing estimate by simply advancing a few samples ahead to avoid locking to the wrong path. We find through extensive simulation that by using that timing estimate whose value is 10-sample earlier than the original coarse timing estimate is enough to overcome the multipath effect. The lock-in probability (no ISI) then becomes very high. After finishing the coarse timing synchronization and meantime fractional frequency offset synchronization, one needs to evaluate the angle of $\gamma(\hat{\theta})$. Figs. 2.14 and 2.15 show respectively the learning curves of of the conventional and modified coarse frequency synchronizers. Our modified fast coarse frequency synchronizer renders

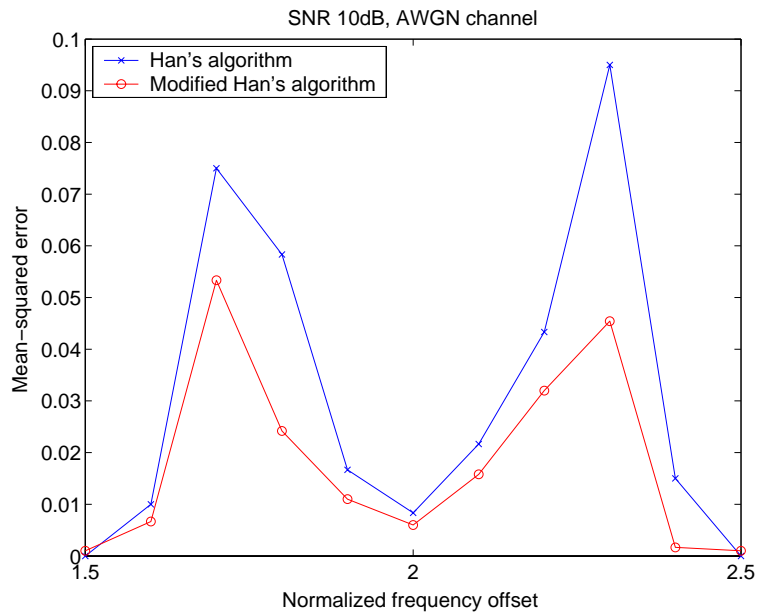
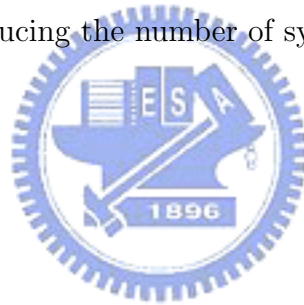


Figure 2.13: The MSE performance of the coarse frequency synchronizer where χ ranges from 1.5 to 2.5 (6.696KHz to 11.16KHz in 2K mode).

a superior performance while reducing the number of symbols required.



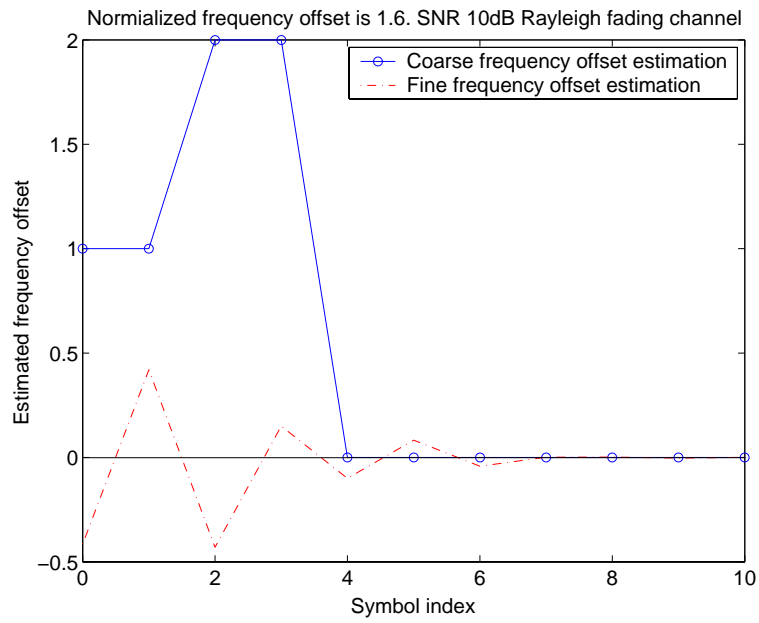


Figure 2.14: Learning curves of the conventional carrier frequency synchronizer.

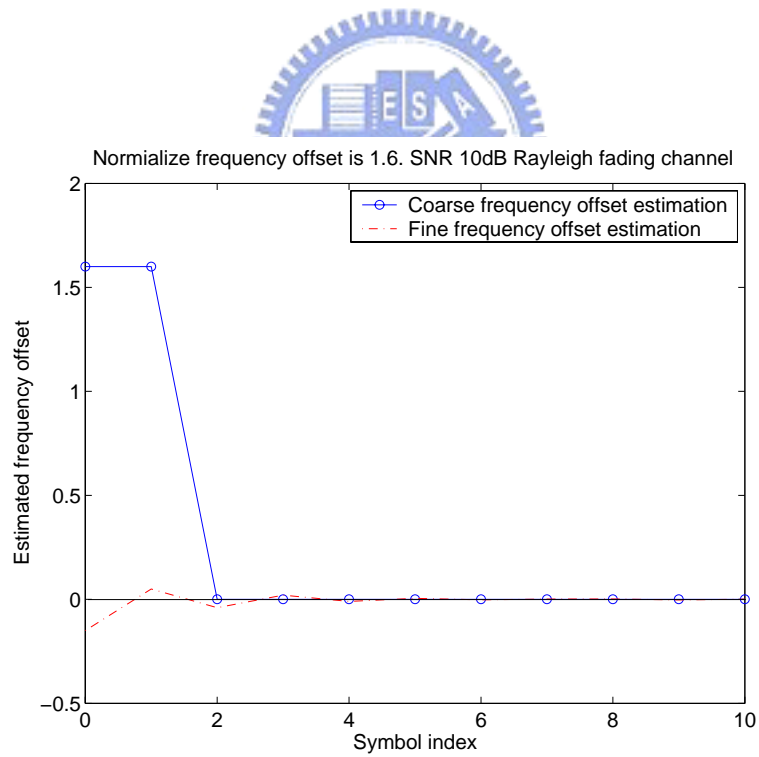


Figure 2.15: Learning curves of modified fast carrier frequency synchronizer.

Chapter 3

Channel Estimation

3.1 Fundamental of OFDM Channel Estimate

In this chapter we study methods that use the scatter pilot to estimate the channel frequency response. Most channel estimation methods for OFDM transmission systems have been developed under the assumption of a static or slow fading channel, where the channel transfer function remains stationary within at least one OFDM data frame. In practice, the channel transfer function of wideband radio channel might have significant changes even within one OFDM data frame. Therefore, it is preferable to estimate channel characteristic based on the pilots in each individual OFDM data frame instead of many adjacent frames.

Fig 1.8 shows that the modulated data $\{S(k)\}$ are transformed and multiplexed into the time-domain sequence $\{s(n)\}$ by inverse DFT

$$s(n) = \sum_{k=0}^{N-1} S(k)e^{j2\pi kn/N}, \quad n = 0, \dots, N-1 \quad (3.1)$$

where N is the number of subcarriers. The received signal can be represented by

$$r(n) = s(n) \otimes h(n) + w(n). \quad (3.2)$$

where $h(n)$ is the impulse response of channel and $w(n)$ is the AWGN. The channel impulse response can be expressed as

$$h(n) = \sum_{i=0}^{M-1} h_i e^{j2\pi f_{D_i} T n/N} \delta(n - \tau_i). \quad (3.3)$$

where M is the total number of propagation paths, h_i , f_{D_i} and τ_i are the complex weight, Doppler shift and normalized relative delay of the i th path (i.e., the true delay minus the shortest path delay then divided by T). The received pilot signals $\{R_p(k)\}$ are extracted from $\{R(k)\}$ and the channel transfer function $\{H(k)\}$ can be obtained from the information carried by $\{H_p(k)\}$. With the knowledge of the channel response $\{H(k)\}$, the transmitted data samples $\{S(k)\}$ can be detected by simply dividing the received frequency domain sample by the estimated channel response

$$\hat{S}(k) = \frac{R(k)}{\hat{H}(k)}, \quad k = 0, 1, \dots, N - 1 \quad (3.4)$$

where $\hat{H}(k)$ is an estimate of $H(k)$. After signal de-mapping and decoding, the source binary information sequence is reconstructed at the receiver. The DVB-T standard assigns pilots in the frequency domain and their arrangement is suitable for aiding synchronization and channel estimation in fading channel. The pilot signals $\{S_p(m)\}$ is $\pm \frac{4}{3}$ generated using the pseudo random binary sequence (PRBS) whose generator polynomial is given by $X^{11} + X^2 + 1$; see Fig. 3.1. Let $\mathbf{H}_p = [H_p(0) H_p(1) \dots H_p(N_p - 1)]^T$ be

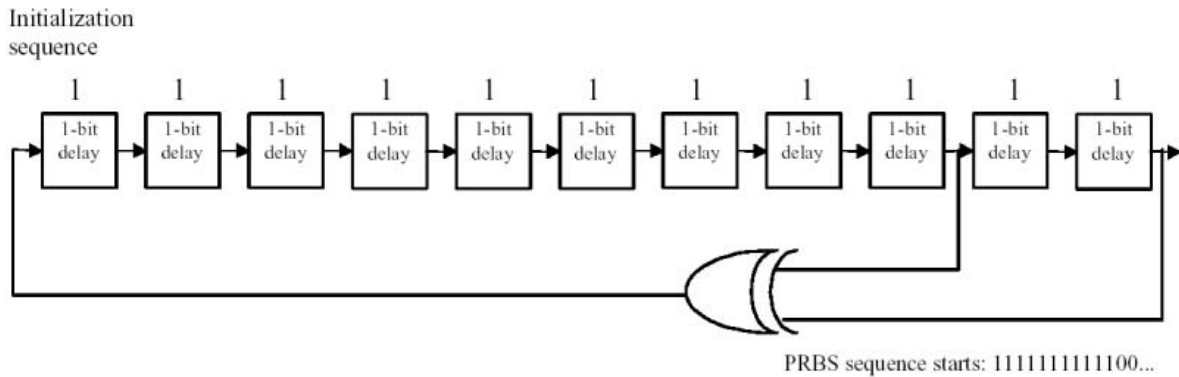


Figure 3.1: Generation of PRBS sequence.

the channel response of at pilot subcarrier and $\mathbf{R}_p = [R_p(0) R_p(1) \dots R_p(N_p - 1)]^T$ be the corresponding received vector. The received pilot signal vector can be expressed as

$$\mathbf{R}_p = \mathbf{S}_p \cdot \mathbf{H}_p + \mathbf{I}_p + \mathbf{W}_p, \quad (3.5)$$

where

$$\mathbf{S}_p = \begin{bmatrix} S_p(0) & & 0 \\ & \ddots & \\ 0 & & S_p(N_p - 1) \end{bmatrix} \quad (3.6)$$

\mathbf{I}_p and \mathbf{W}_p are the inter-carrier interference (ICI) and the AWGN components in pilot locations. The conventional least squares (LS) channel estimate is given by

$$\hat{\mathbf{H}}_{p,ls} = \mathbf{S}_p^{-1} \mathbf{R}_p = \left[\begin{array}{ccc} R_p(0) & R_p(1) & \dots & R_p(N_p - 1) \\ S_p(0) & S_p(1) & & S_p(N_p - 1) \end{array} \right]^T \quad (3.7)$$

The LS estimate on data positions are obtained through interpolating $\hat{\mathbf{H}}_{p,ls}$ and is very sensitive to Gaussian noise and ICI. The piecewise-linear interpolation method has been studied in [9]. In the linear interpolation algorithm, two successive pilot subcarriers are used to determine the channel response for data subcarriers that are located in between the pilots. For data subcarrier k , $mL \leq k \leq (m+1)L$, L is the distance between two pilots. The estimated channel response using linear interpolation method is given by

$$\begin{aligned} \hat{H}(k) &= \hat{H}(mL + l) = \left(1 - \frac{l}{L}\right) \hat{H}_p(m) + \frac{l}{L} \hat{H}_p(m+1) \\ &= \hat{H}_p(m) + \frac{l}{L} (\hat{H}_p(m+1) - \hat{H}_p(m)), \quad 0 \leq l \leq L \end{aligned} \quad (3.8)$$

Theoretically, using higher-order polynomial interpolation will fit the channel response better than the linear interpolation but the computational complexity grows as well. Using the second-order polynomial interpolation yields

$$\hat{H}(k) = \hat{H}(mL + l) = C_1 \hat{H}_p(m-1) + C_0 \hat{H}_p(m) + C_{-1} \hat{H}_p(m+1), \quad (3.9)$$

where

$$\begin{cases} C_1 &= \frac{\alpha(\alpha+1)}{2} \\ C_0 &= -(\alpha-1)(\alpha+1) \\ C_{-1} &= \frac{\alpha(\alpha-1)}{2} \end{cases} \quad (3.10)$$

and $\alpha = l/N$.

3.2 DVB-T channel model

Fig. 3.2 plots a static version of DVB-T channel impulse response whose path gains and phases are given in Table 3.1. In simulation, we have used Rayleigh fading channel. DVB-T can operate at a single frequency networks (SFN) in which the same program is broadcasted simultaneously at two or more sites using the same frequency. The SFN architecture fills gaps within or extends the service provided by a single transmitter. This technique is applicable for a DVB-T system due to its resilience to multiple signals. The use of a single channel from multiple transmitters to serve an area allows the efficient use of spectrum. In analogue, multiple channels were required to serve an area and hence reduced the number of services possible. The use of SFN allows more services to be introduced. The maximum delay of SFN is assumed to be smaller than guard interval. In our simulation, we used two identical channel profiles to model a SFN channel, see Fig. 3.4.

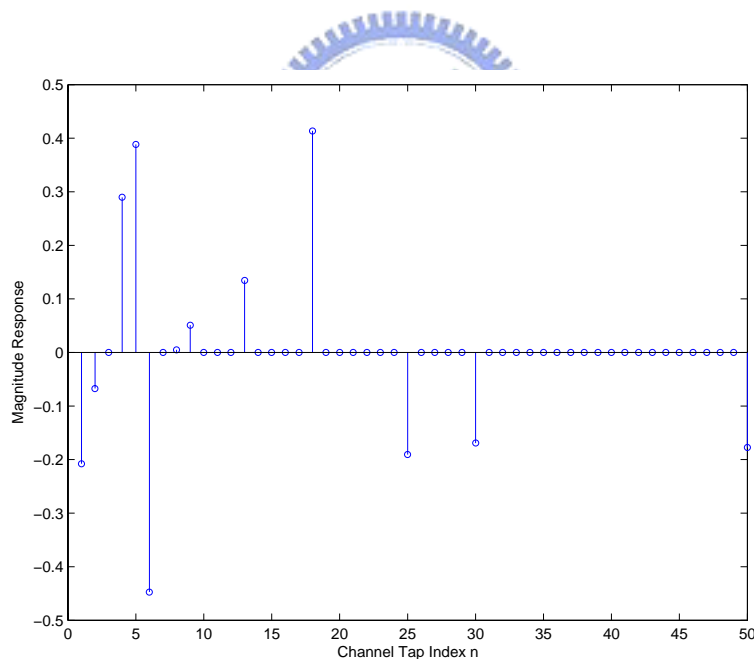


Figure 3.2: A typical DVB-T channel's impulse response with a duration of 12 taps.

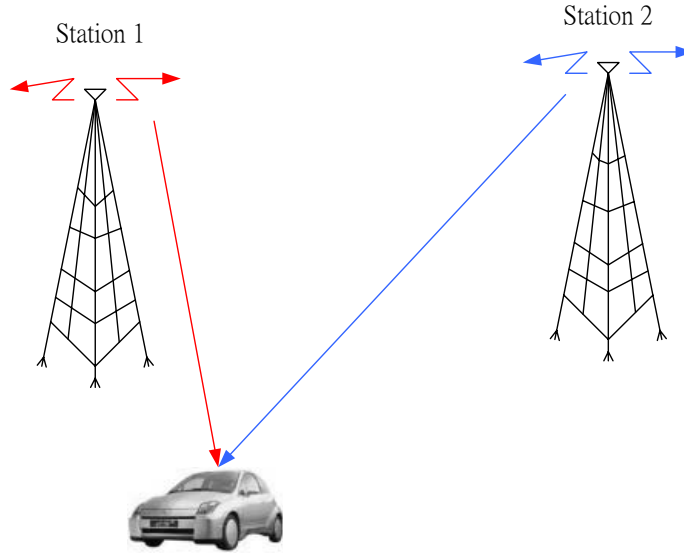


Figure 3.3: The DVB-T single frequency network (SFN) concept.

3.2.1 Jakes model

Jakes model [10] is a very popular channel model for mobile multipath channels that takes into account the Doppler effect and is based on the assumptions that the receiver is moving at speed v while the arrival angles of multipath components are uniformly distributed. The time correlation of the channel is then given by

$$R(\Delta t) = J_0(2\pi \cdot \Delta t \cdot f_d) \quad (3.11)$$

where Doppler frequency $f_d = v \cdot f_c/c$, f_c is the carrier frequency and c is the speed of light. $J_0(x)$ is the zero-*th* order Bessel function of the first kind.

3.3 Phase compensation

In Chapter 2, we mentioned that the residual timing error tends to introduce phase rotation that leads to model mismatch errors for interpolation-based channel estimation.

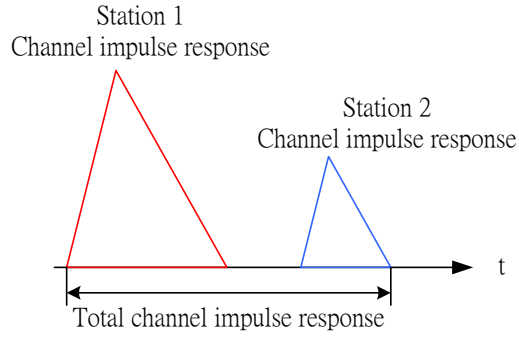


Figure 3.4: Combined impulse response of a DVB-T single frequency network with two stations.

This model mismatch error is an increasing function of the timing error

$$\hat{\theta}_e = \sum_{m=0}^{N_p-2} w(m) \angle \hat{H}_p^*(m) \hat{H}_p(m+1) \quad (3.12)$$

where N_p is the number of pilot subcarrier and

$$w_m = \frac{\frac{3}{2}N_p}{N_p^2 - 1} \left\{ 1 - \left[\frac{m - (\frac{N_p}{2} - 1)}{\frac{N_p}{2}} \right]^2 \right\} \quad (3.13)$$

Recall that the simple estimator of [8] based on the phase estimates are

$$\hat{\theta}_e = \frac{1}{N-1} \sum_{m=0}^{N_p-2} \angle \hat{H}_p^*(m) \hat{H}_p(m+1). \quad (3.14)$$

Given $\hat{\theta}_e$, the channel responses at pilot locations are updated via

$$\begin{aligned} \tilde{H}_p(m) &= \hat{H}_p(m) \cdot e^{j\hat{\theta}_e m} \\ &\approx H_p(m) + E'_{H_p}(m) \end{aligned} \quad (3.15)$$

After this phase compensation, the channel responses at data carriers are interpolated by using linear or higher-order polynomial interpolation and the resulting estimates $\tilde{H}_d(k)$ is refined as

$$\hat{H}_d(k) = \tilde{H}_d(k) \cdot e^{-jk\frac{\hat{\theta}_e}{L}}. \quad (3.16)$$

Because the timing error is compensated by (3.15), the model mismatch error is reducing considerably.

Delay (OFDM samples)	Gain	Phase(rad)
0	0.2478	-2.5649
1	0.1287	-2.1208
3	0.3088	0.3548
4	0.4252	0.4187
5	0.49	2.7201
7	0.0365	-1.4375
8	0.1197	1.1302
12	0.1948	-0.8092
17	0.4187	-0.1545
24	0.317	-2.2159
29	0.2055	2.8372
49	0.1846	2.8641

Table 3.1: Path gains and phase rotations associated with the DVB-T channel impulse response of Fig. 3.2.

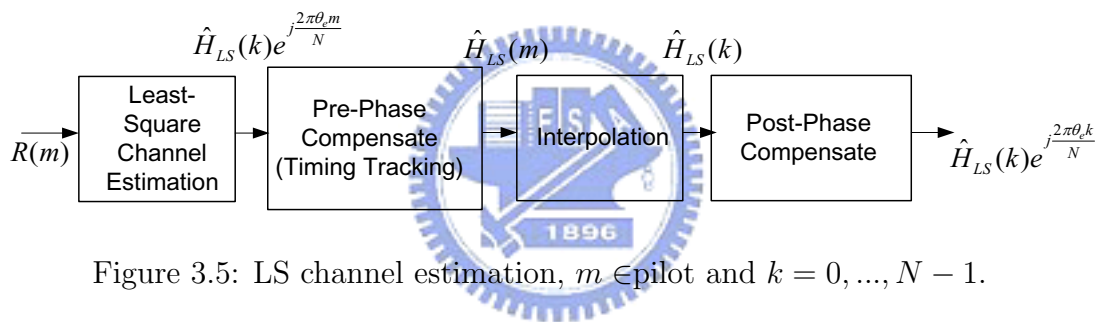


Figure 3.5: LS channel estimation, $m \in \text{pilot}$ and $k = 0, \dots, N - 1$.

3.4 Transform-domain channel estimation algorithm

A channel estimation based on transform-domain processing was proposed in [11]. This method employs lowpass filtering in the transform domain so that intercarrier interference and additive white Gaussian noise components in the received pilots are significantly reduced.

Rewriting (3.7) as

$$\hat{H}_{p,ls}(m) = H_p(m) + \frac{[I(m) + W(m)]}{X_p(m)}, \quad m = 0, \dots, N_p - 1 \quad (3.17)$$

Since both ICI and AWGN in time domain are zero mean random processes, the noise

component $\frac{I(m)+W(m)}{X_p(m)}$ in (3.17) is a zero mean Gaussian random process as well. Variation of the true frequency transfer function $H_p(m)$ within one or a few OFDM frames is usually very slow with respect to the pilot subcarrier index m but that of the noise component $\frac{I(m)+W(m)}{X_p(m)}$ is fast and large. We can use this property to separate the two components by employing a transform-domain lowpass filter where the transform domain refers to the “frequency domain” in DFT-IDFT transformations. Therefore, a sequence in the frequency domain is the spectral sequence of its counterpart in the frequency. The argument p of the transform domain can be viewed as the ”frequency” which reflects the variation rate of a frequency domain function. The transform domain representation of $\hat{H}_{p,ls}(m)$ becomes

$$\hat{G}_p(p) = \sum_{m=0}^{N_p-1} \hat{H}_{p,ls}(m) e^{-j2\pi mp/N_p}, \quad (3.18)$$

where $p \in [0, N_p - 1]$ is the transform domain index. Fig. 3.6 plots the frequency responses of two channel conditions, one with noise and Doppler shift ((b)) and another one without ((a)) As expected, the signal component in $\hat{G}_p(p)$ is located at the lower ”frequency” (around $p = 0$ and $p = N_p - 1$) region, while the noise component is spread over the full band ($p = 0, \dots, N_p - 1$).

The lowpass filtering can be realized by simply setting the samples in the “high frequency” band to zero, that is

$$\tilde{G}_p(p) = \begin{cases} \hat{G}_p(p), & 0 \leq p \leq p_c, N_p - p_c \leq p \leq N_p - 1, \\ 0, & \text{otherwise} \end{cases} \quad (3.19)$$

where p_c is the cutoff frequency of the filter in the transform domain. Such a low-pass filtering reduces the noise component by an order $2p_c/N_p$.

3.4.1 Cutoff frequency

The cutoff frequency p_c of the transform domain lowpass filter is an important parameter that affects the accuracy of the channel estimation. The optimal cutoff frequency depends on the channel condition and, therefore, an approach is needed to select

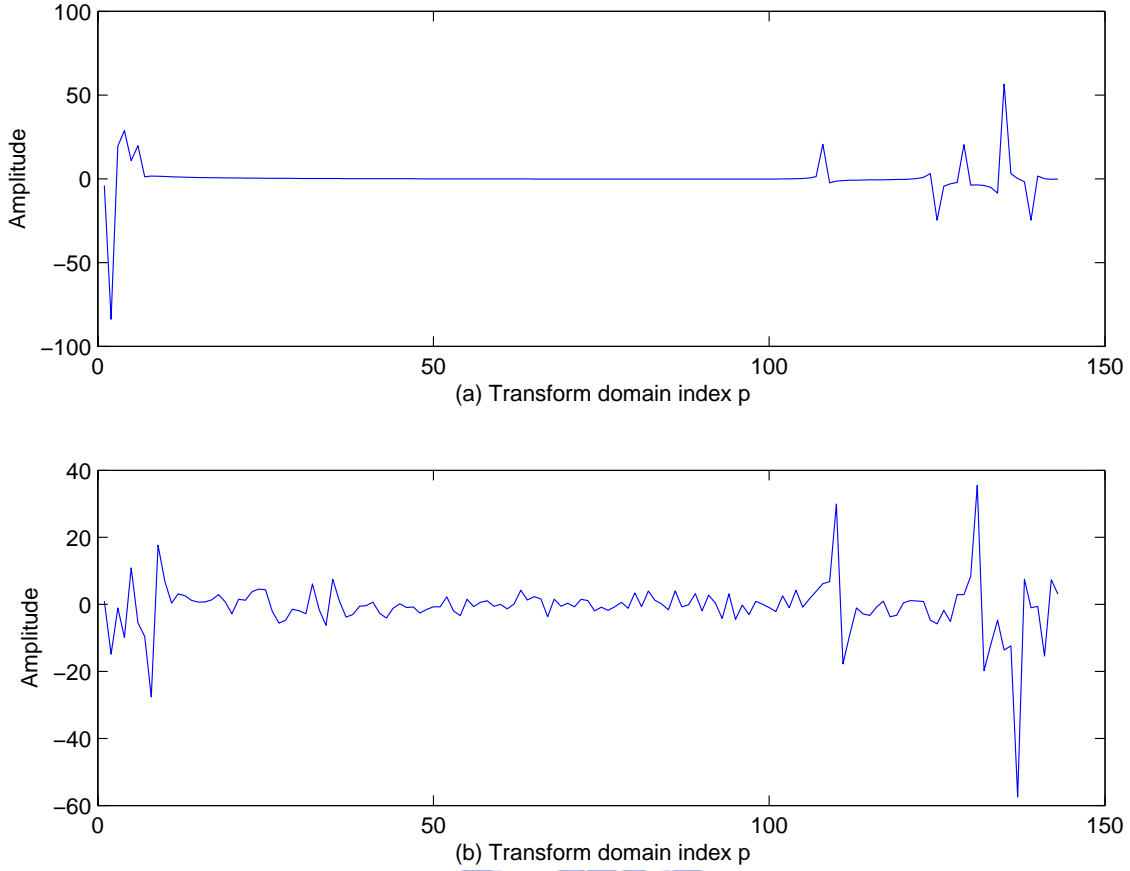


Figure 3.6: A typical transform domain response $\hat{G}_p(p)$ when (a) AWGN and Doppler shift are absent (i.e., noiseless static channel) and (b) SNR = 5 dB, Doppler frequency = 90 Hz.

p_c dynamically by tracking the channel variation. Comparing parts (a) and (b) of Fig. 3.6, we find that most of the energy concentrates at the lower frequency region where the desired components dominate. It is thus suggested that p_c be determined from the following relation

$$\frac{\left[\sum_{p=0}^{p_c} |\bar{G}_p(p)|^2 + \sum_{p=N_p-p_c}^{N_p-1} |\bar{G}_p(p)|^2 \right]}{\sum_{p=0}^{N_p-1} |\bar{G}_p(p)|^2} = \Lambda \quad (3.20)$$

where the numerator is the energy in the passband, the denominator represents the total energy, $\Lambda \in [0.9, 0.95]$, and $\bar{G}_p(p)$ is the average value of $\hat{G}_p(p)$ of the present data symbol and 10 previous ones.

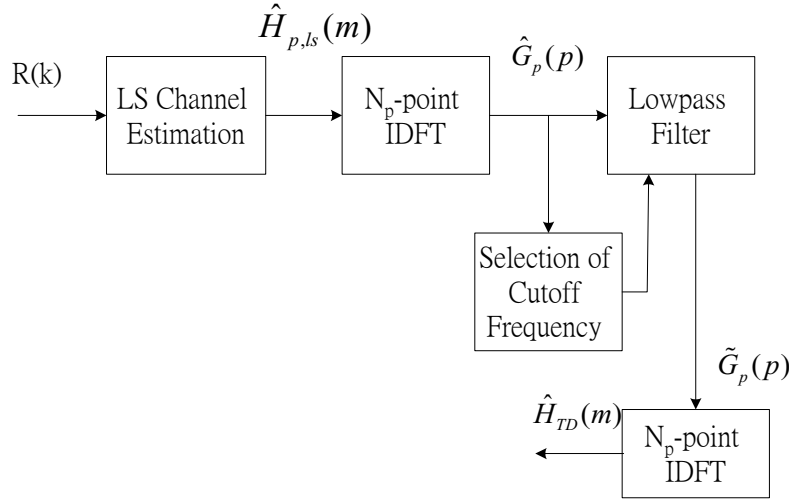


Figure 3.7: Block diagram of a channel estimation algorithm based on transform-domain processing; $m \in \text{pilots}$ and $k = 0, \dots, N - 1$ and $p = 0, \dots, N_p - 1$.

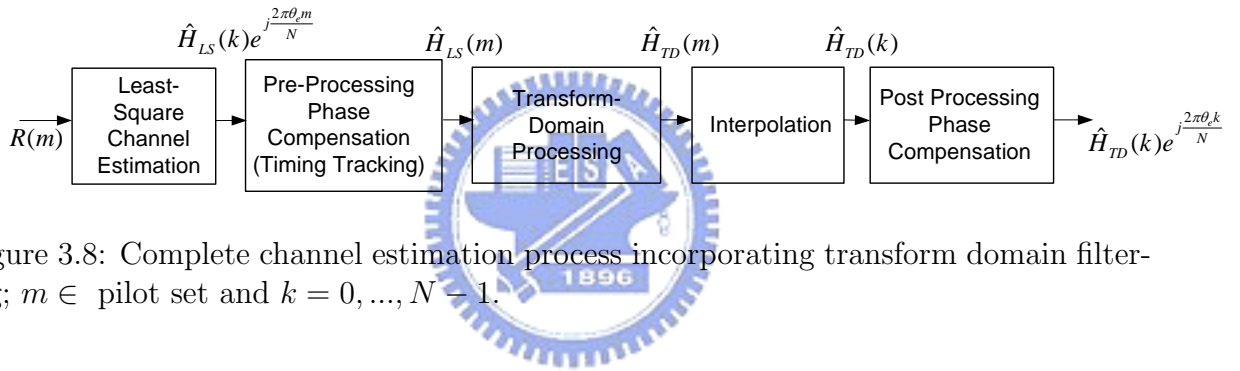


Figure 3.8: Complete channel estimation process incorporating transform domain filtering; $m \in \text{pilot set}$ and $k = 0, \dots, N - 1$.

3.5 Model-based channel estimation

We now examine the effectiveness of the novel model-based estimation method of [12] for estimating DVB-T channels. The LS channel estimation is given by

$$\hat{H}_{p,ls}(m, n) = \frac{R_p(m, n)}{X_p(m, n)} = H_p(m, n) + \frac{W(m, n) + I(m, n)}{X_p(m, n)}, \quad (3.21)$$

where p indicate the pilot positions. $H(m, n)$, $X_p(m, n)$ and $R_p(m, n)$ denote the channel response, transmitted signal and received samples at the m th subcarrier during the n th symbol interval. The channel responses $H(m, n)$ can be viewed as a sampled version of the two-dimension continuous complex fading process $H(f, t)$. We choose a operating

region in the time-frequency plane and approximate the sampled fading process $H(m, n)$ in this region by the quadrature surface

$$f(x, y) = ax^2 + bxy + cy^2 + dx + ey + f, \quad (3.22)$$

where the coefficients (a, b, c, d, e, f) are determined such that

$$\sum_{(m,n) \in \text{pilot tones}} \left| \hat{H}_{p,ls}(m, n) - f(m, n) \right|^2 \quad (3.23)$$

is minimized. Rewriting (3.25) in more compact form

$$\sum_{(m,n) \in \text{pilot tones}} \left| \hat{H}_{p,ls}(m, n) - \mathbf{q}_{mn}^T \mathbf{c} \right|^2 \quad (3.24)$$

where $\mathbf{c}^H = (a, b, c, d, e, f)$ is the coefficient vector and $\mathbf{q}_{mn}^T = (m^2, mn, n^2, \dots, m, 1)$ is the pilot location vector. We shall only consider the case of one-dimensional (1-D) regression model.

$$\hat{H}_{\text{model}}(m) = c_0 + c_1 m + c_2 m^2, \quad 0 \leq m < L, \quad (3.25)$$

where L is the block length.

$$\hat{\mathbf{c}} = \arg \min_c \sum_{m=0}^{L-1} \left| \hat{H}_{p,ls}(m) - \mathbf{q}_m^T \mathbf{c} \right|^2 \quad (3.26)$$

where $\mathbf{c}^H = (a, b, c)$ is the coefficient vector and $\mathbf{q}_m^T = (m^2, m, 1)$ is the pilot location vector. Fig. 3.9 indicates the fitting processing. We can write (3.26) more concisely by

$$\hat{\mathbf{c}} = \arg \min_c \left\| \hat{\mathbf{H}}_{p,ls} - \mathbf{Q} \mathbf{c} \right\|^2 \quad (3.27)$$

where $\hat{\mathbf{H}}_{p,ls} = (\hat{H}_{p,ls}(0), \hat{H}_{p,ls}(1), \dots, \hat{H}_{p,ls}(L-1))^T$ and

$$\mathbf{Q} = \begin{pmatrix} \mathbf{q}_0^T \\ \mathbf{q}_1^T \\ \vdots \\ \mathbf{q}_{L-1}^T \end{pmatrix} = \begin{pmatrix} 1 & 0 & 0 & \cdots & 0 \\ 1 & 1 & 1 & \cdots & 1 \\ 1 & 2 & 2^2 & \cdots & 2^d \\ \vdots & \vdots & \vdots & \ddots & \vdots \\ 1 & (L-1) & (L-1)^2 & \cdots & (L-1)^d \end{pmatrix}. \quad (3.28)$$

Note that from (3.25) $\mathbf{Q}\mathbf{c} = (\hat{H}_{model}(0), \hat{H}_{model}(1), \dots, \hat{H}_{model}(L-1))^T = \hat{\mathbf{H}}_{model}$ is the new estimate of channel impulse response. By solving (3.27), the coefficients of the regression polynomial is

$$\hat{\mathbf{c}} = (\mathbf{Q}^T \mathbf{Q})^{-1} \mathbf{Q}^T \hat{\mathbf{H}}_{p,ls}, \quad (3.29)$$

and we obtain the new estimates

$$\hat{\mathbf{H}}_{model}(m) = \mathbf{q}_m^T \hat{\mathbf{c}}. \quad (3.30)$$

$$\hat{\mathbf{H}}_{model} = \mathbf{Q}\hat{\mathbf{c}} = \mathbf{Q}(\mathbf{Q}^T \mathbf{Q})^{-1} \mathbf{Q}^T \hat{\mathbf{H}}_{p,ls} = \mathbf{V}\hat{\mathbf{H}}_{p,ls}, \quad (3.31)$$

where

$$\mathbf{V} = \mathbf{Q}(\mathbf{Q}^T \mathbf{Q})^{-1} \mathbf{Q}^T. \quad (3.32)$$

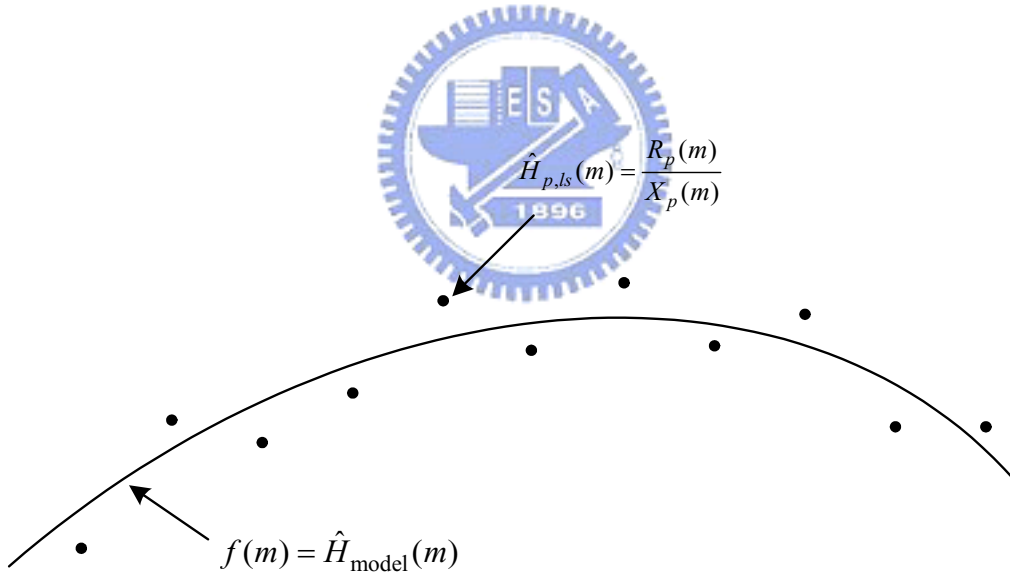


Figure 3.9: Indication of the least-squared-fitting processing.

According to [12], we know that the model-based channel estimation gives better performance when uniform pilot structure is in place. However, as shown in Fig. 1.6,

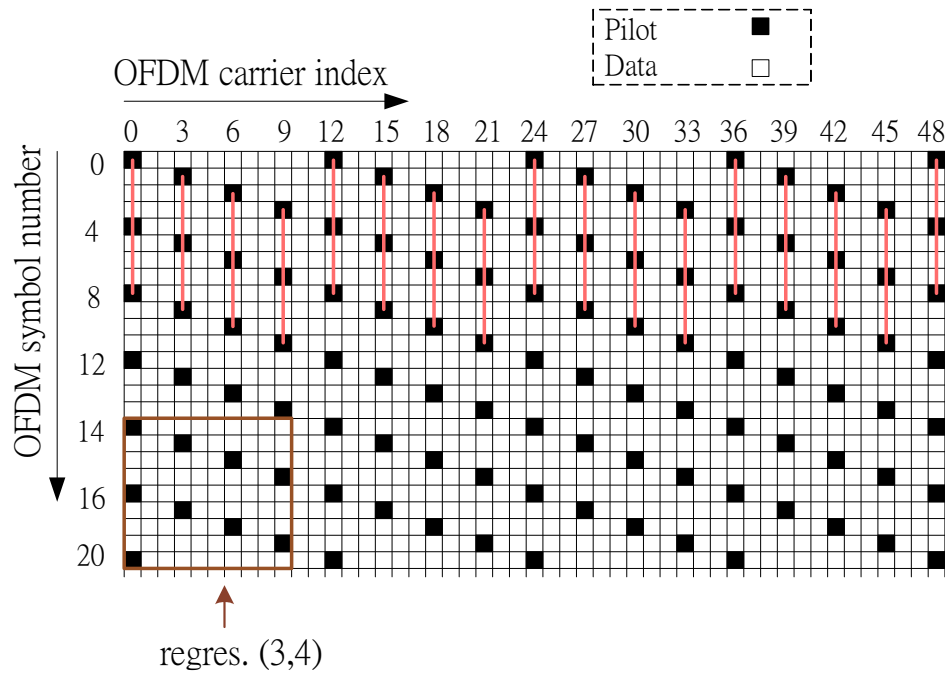


Figure 3.10: DVB-T pilot symbol distribution in time-frequency. In the bottom of this figure, `regres.(3,4)` means that use 3 pilots in time domain and 4 pilots in frequency domain to make regression model.

the pilot distribution in DVB-T is not uniform, we modify the model-based approach by first estimate the channel responses at selected subcarriers using a 1D model. Regarding the recovered channel responses as pilots, we then apply the 2D model-based procedure for solving the remaining data locations; see Fig. 3.10).

3.6 2-D model-based channel estimate with transform-domain processing

Shown in Fig. 3.11 is a block diagram that represents an improved channel estimator, concatenating the transform-domain processing algorithm with the 2-D model-based channel estimator. As the transform-domain processing (TDP) unit suppresses the ICI and AWGN effects, the following 2-D model-based channel estimation unit stands a much better chance to find a curve that comes very close to real channel response.

We therefore expect this two-stage algorithm to give enhanced performance for DVB-T systems. N_t is the transform size (FFT size), we can change N_t to reduce the complexity

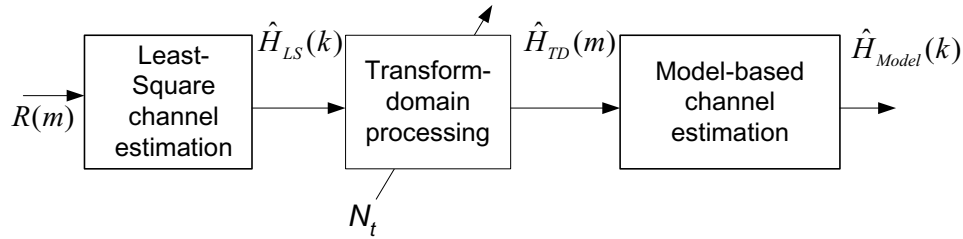


Figure 3.11: Block diagram of a two-stage channel estimator that consists of a TDP unit and a model-based channel estimation unit.

of our proposed algorithm. In our simulation, we select 3 different number for N_t , thus, N_p , 128 and 64, see Fig. 3.15, where N_p is the number of pilot tones in a OFDM symbol. If $N_t = N_p$ means all pilots will input to TDP for suppress all kinds of interference.

3.7 Computational complexity

LS channel estimation needs N_p complex division or $5N_p$ multiplication in a symbol. Two addition and two real multiplication are needed per subcarrier in the linear interpolation. Thus, use LS with linear interpolation needs $5N_p + 2N$ real multiplications in a OFDM symbol. In 2K mode DVB-T system, it requires about 2 complex multiplication per subcarrier.

The channel estimation based on transform-domain processing uses two FFTs to estimate the channel response. the both of size is N_p (if we used FFT interpolation the size of FFT is N_p and N). By using the decimation-in-frequency radix-2 implementation of FFT, the total number complex multiplications required is roughly $2N_p \log_2 N_p$. By using the parameters in 2K mode DVB-T system, the transform-size is replaced by 256. It requires at least $2N$ complex multiplication and $2N$ real multiplications in an OFDM symbol, TDP (by using linear interpolation) requires about 4 complex multiplication

per subcarrier.

It is preferred to use (3.29) and (3.30) in calculation for complexity consideration of regression model. The computational algorithm is

$$\hat{\mathbf{c}} = \mathbf{P}\hat{\mathbf{H}}_{p,ls}, \quad (3.33)$$

$$\hat{\mathbf{H}}_{\text{model}}(m) = \mathbf{q}_m^T \hat{\mathbf{c}}, \quad (3.34)$$

where $\mathbf{P} = (\mathbf{Q}^T \mathbf{Q})^{-1} \mathbf{Q}^T$ is a constant matrix. The dimension of \mathbf{P} is $(d+1) \times L$, so to obtain \mathbf{c} we need $2(d+1)L$ real multiplication since \mathbf{P} is real. Calculating each channel response at the data tone using (3.34) needs $2(d+1)$ real multiplication. Since there are $L(r-1)$ data tones, where r is the subcarrier spacing of pilot tone, we need totally $5L + 2L(r-1)(d+1) + 2(d+1)L$ real multiplications. Average over $L(r-1)$ data locations, we need less than $4(d+1)$ real multiplication. We conclude that in estimating each $\hat{H}_{\text{model}}(m)$ at the data tone, we need less than $(d+1)$ complex multiplication on the average. Thus, it requires about 3 complex multiplication per subcarrier. Our proposed 2-D regression model with TDP requires about 4 complex multiplication if the transform size is 128. Use 2-D regression $(3, L_f)$ needs $7N$ memory to store those symbols information, and 2-D regression $(4, L_f)$ needs $11N$ memory. By using 1-D channel estimation is not need any extra memory to save symbol information.

3.8 Numerical examples

Numerical behavior of various channel estimates is reported in this section. We assume that QPSK modulation with a rate 1/2 convolutional code is used and perfect timing (frame) recovery is achieved. The 2-D model-based channel estimation with TDP (2D-MB-TDP) algorithm, as indicated in Fig. 3.12, has the best performance amongst those channel estimation algorithms examined. Fig. 3.13 show that the same conclusion holds when Doppler and noise are presented and the system operates in a SFN channel with r.m.s. delay spread of $5.13\mu s$ (or equivalently 48 samples). The improvement

with respect to 1D algorithms becomes very significant in this case. When delay spread increases, the coherent bandwidth decreases so that the pilots in frequency domain is not dense enough to properly interpolate the channel response across the whole transmission band. Use a 2-D channel estimation algorithm help overcoming this difficulty.

In Figs. 3.13 and 3.14, $\text{regres.}(L_t, L_f)$ denotes that the time-frequency region selected for 2D modelling contains L_t time pilots and L_f frequency pilots; see Fig. 3.11. These curves show that it is better to use smaller frequency domain modelling width (fewer frequency pilots) in modelling the channel impulse response. Fig. 3.15 shows that the price we pay for reducing the FFT window size N_t is negligible. Since in the $2K$ mode, there are 143 pilots in frequency domain which is not a power of 2, we use 256 points or 128 points FFT instead.

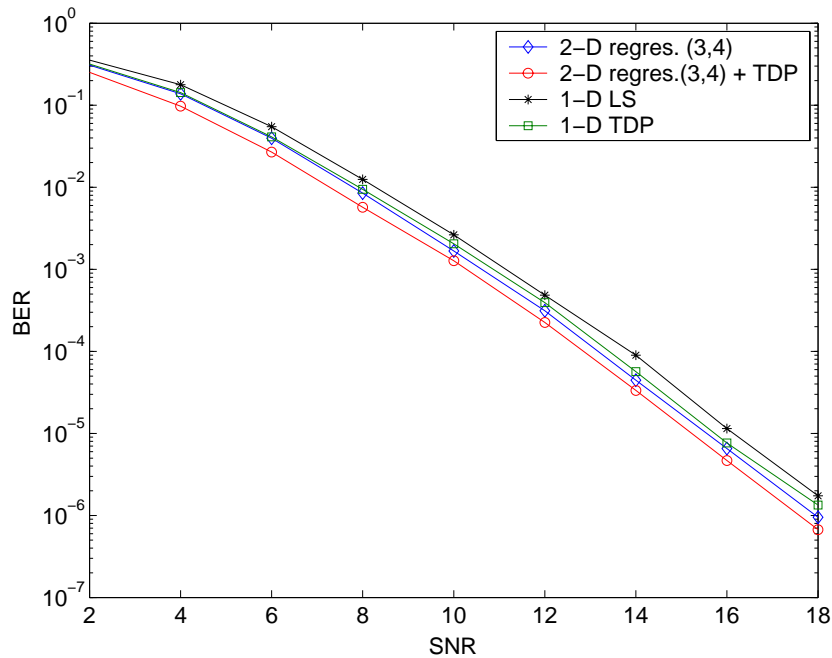


Figure 3.12: BER performance comparison of various channel estimates; zero Doppler shift, r.m.s. delay spread = $1.36 \mu s$.

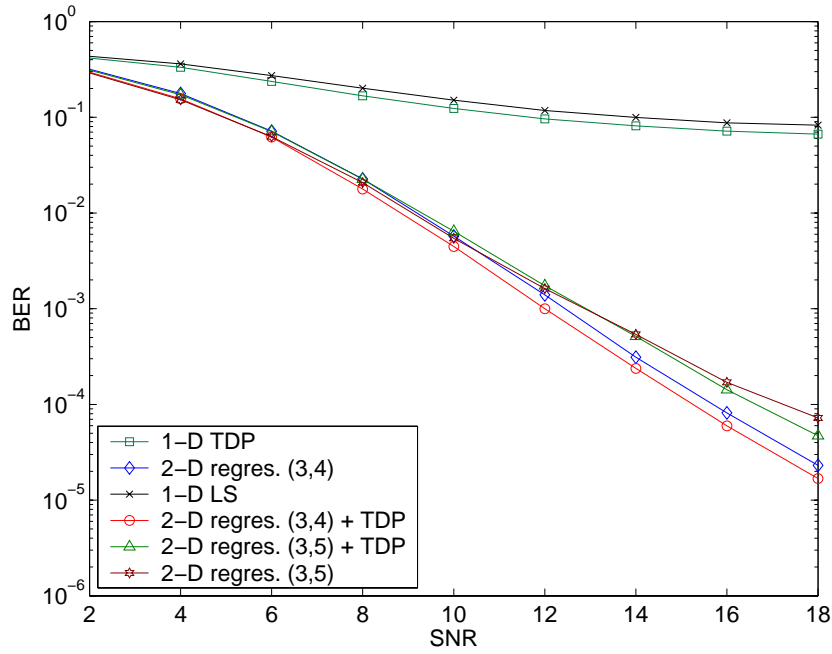


Figure 3.13: BER performance comparison of various channel estimates; Doppler frequency = 88 Hz, r.m.s. delay spread = $5.13\mu s$.

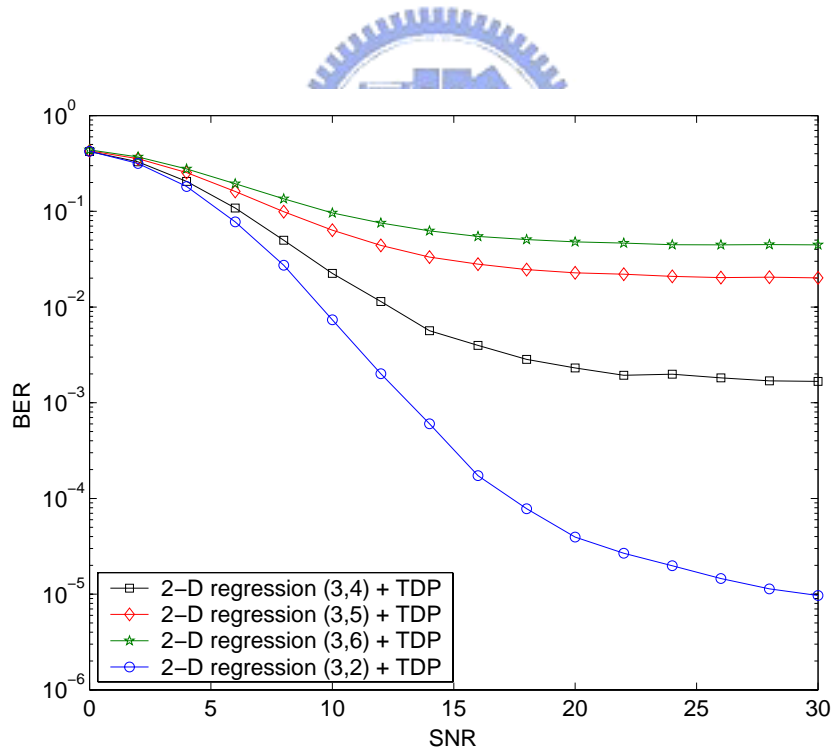


Figure 3.14: The effect of the 2D model size on the BER performance; Doppler shift = 88 Hz, r.m.s. delay spread = $9.1245\mu s$.

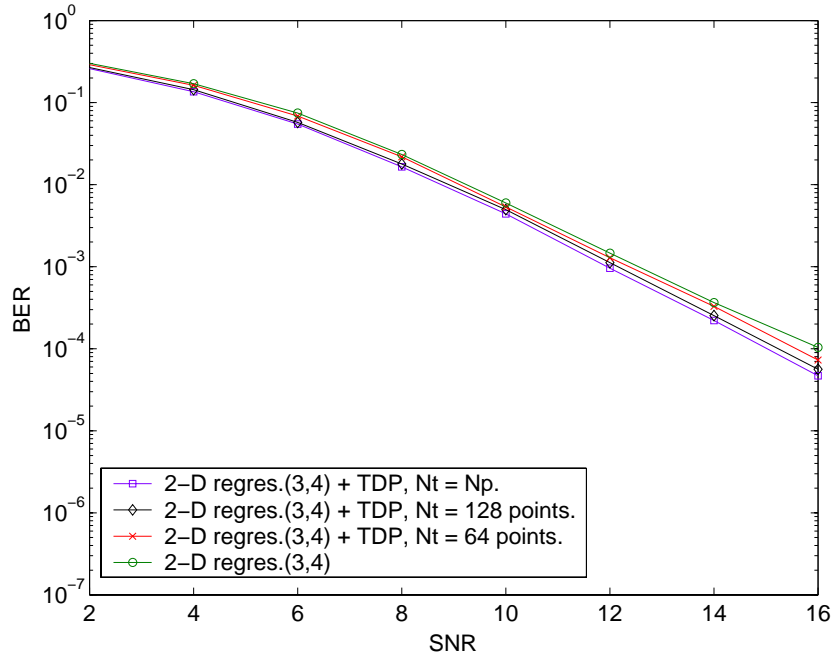


Figure 3.15: The effect of the FFT window size on the BER performance; Doppler frequency = 88 Hz, r.m.s. delay spread = $1.36\mu s$.

Chapter 4

Impulse Noise Suppression

4.1 Background

A radio communication waveform is likely to suffer from several kinds of impairments. Most of them, e.g. thermal, atmospheric, or galactic noise, can be represented by a Gaussian model. However, man-made noise that appears in urban environments created by the electrical self-starter of cars, power lines, heavy current switches, arc welders, fluorescent lights, etc., cannot be assumed to be Gaussian. As they all have a short duration nature, they are often represented by an impulsive model. Taking the occurring instances of these shot noise into account, we model the impulse noise (IN) as a random train of pulses with a very wideband power spectral density. Detailed impulse noise model in the next section. To eliminate or at least suppress the influence of IN, one has to be able to detect its presence. Detecting the arrivals of impulse noise is discussed in Section 4.3. We then briefly describe the conventional impulse noise rejection method—the blanking method in Section 4.4. New IN suppression algorithms are given in Sections 4.5 and 4.6.

4.2 Impulse noise model

We use the IN model based on the Sanchez's [15] measurements in which two outdoor environments referred to as noisy place and quiet place, respectively are considered. We

will limit our investigation to the noisy place IN model given by

$$i(t) = \sum_i a_i \prod w_i(t - t_i) \quad (4.1)$$

This model has three random variables, namely, the pulse duration, pulse amplitude and elapsed time between pulses. The distribution of elapsed time between pulses follows a Gamma distribution, but none of the distribution function is adequate to model the pulse amplitudes or the pulse duration that said by [15]. We choose a static impulse noise model and for the worst-case consideration, we assume that the impulse burst occurs exactly once in every 8th OFDM symbol. We want to emphasize that this is a worst-case assumption since almost all IN occurs much less frequently. We choose the Cook pulse [16] to model the pulse amplitude and the pulse duration, see Fig. 4.1.

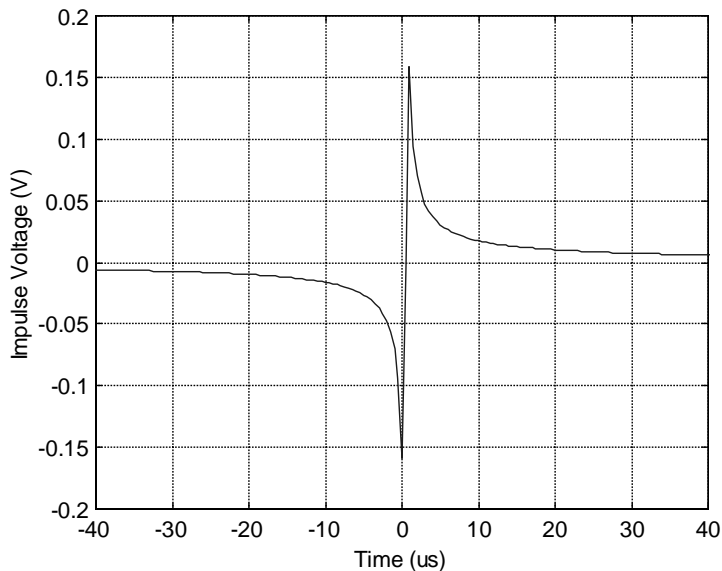


Figure 4.1: The Cook pulse (An impulse noise model).

The received signal $r(n)$ can be expressed as

$$r(n) = s(n) \otimes h(n) + w(n) + i(n) \quad (4.2)$$

where $s(n)$ is transmitted symbol, $h(n)$ is channel impulse response, $w(n)$ is AWGN and $i(n)$ is the impulse noise. All this quantities are assumed to be complex.

4.3 Impulse noise detection

To recover data samples corrupted by IN, the receiver has to be able to determine which samples are IN-corrupted, i.e. to determine if there was an impulse noise in current symbol, and, if yes, to locate its position. The energy detector, also known as radiometer (for detecting the presence of signal or interference), is perhaps the simplest yet efficient algorithm to detect the presence of IN. The sliding window version of the energy detector determines that the IN-corrupted range is $[l_s, l_e]$ where

$$l_s = \min_l \left\{ l : \sum_{k=l}^{l+L-1} y_k^2 > \Upsilon \right\}, \quad l_e = \max_l \left\{ l : \sum_{k=l-L+1}^l y_k^2 > \Upsilon \right\}. \quad (4.3)$$

where L is the mean IN duration.

The simplest way to determine IN location is given by

$$i_p(n) = \begin{cases} 1, & \text{if } r(n) \geq A_0, \\ 0, & \text{otherwise} \end{cases} \quad (4.4)$$

where $i_p(n)$ is the IN indicator function, i.e., it is nonzero and equal to 1 only if the n th sample is interfered by IN and A_0 is a properly selected threshold. To determine if IN is present in the m th OFDM symbol we use the channel state indicator $CSI(m)$

$$CSI(m) = \begin{cases} 1, & \text{if } \sum_{n=m(N+N_g)+N_g}^{(m+1)(N+N_g)-1} i_p(n) \geq A_1, \\ 0, & \text{otherwise} \end{cases} \quad (4.5)$$

where A_1 is the threshold. (4.3) is more complex than (4.4) but properly outperforms the latter as it has more parameters for optimization.

4.4 Blanking method

IN-corrupted data samples are very difficult to recover using any conventional approach because of the large noise magnitude. Thus, it is beneficial to blank [13] the IN-corrupted zone, i.e. the sample values within that zone are set to zero. Even without further processing the blanking alone reduces the distortion caused by IN if the IN detection is perfect. In other words, the advantage of blanking method is replacing the

impulse noise by noise (blanking noise) of smaller magnitude, see Fig. 4.2. Nevertheless, if the signal-to-IN ratio is greater than one the blanking method no longer enjoys such advantage.

$$r(n) = \begin{cases} 0 & \text{if } r(n) \text{ corrupted} \\ r(n) & \text{otherwise} \end{cases} \quad (4.6)$$

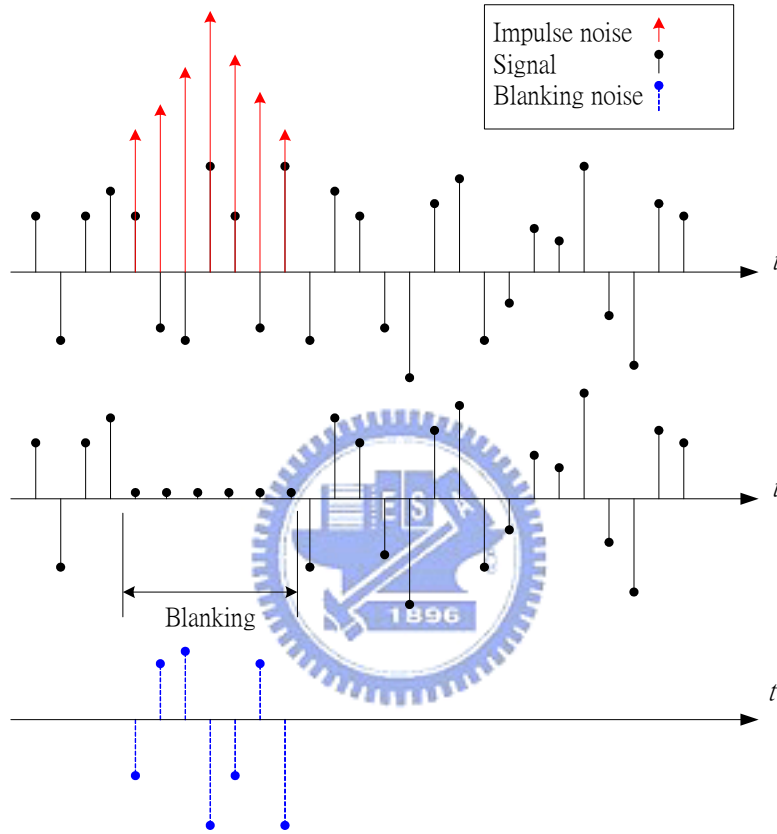


Figure 4.2: Impulse noise and blanking noise

4.5 Decision-aided reconstruction for IN suppression (DARINS)

The blanking method for impulse noise suppression are implemented in the time domain before OFDM demodulation. The decision-aided reconstruction (DAR) [17] algorithm

suppresses IN in the frequency domain. The DAR algorithm was originally proposed for solving the clipping noise problem. Fig. 4.3 explains why impulse noise can be modeled as clipping noise. The frequency domain expression of the IN-corrupted sample sequence

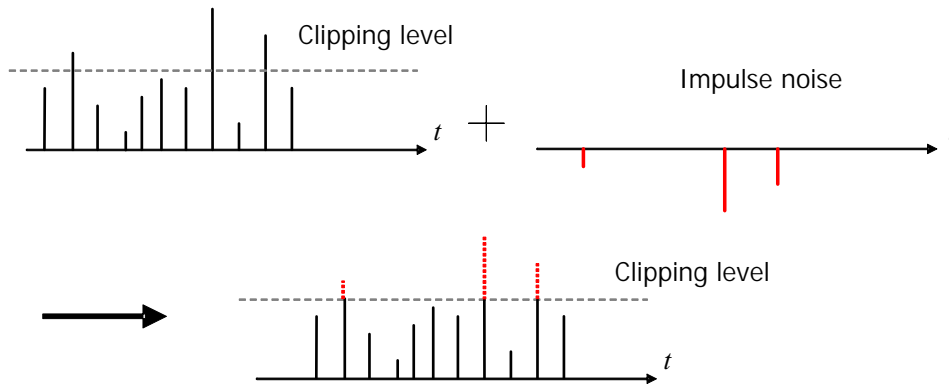


Figure 4.3: Modeling Impulse noise as clipping noise.

is

$$R(k) = S(k)H(k) + W(k) + I(k), \quad k = 0, \dots, N - 1 \quad (4.7)$$

where $S(k)$ is transmitted signal, $H(k)$ is channel response, $W(k)$ is AWGN and $I(k)$ is the DFT of impulse noise, respectively. We now describe the decision-aided reconstruction for impulse noise suppression (DARINS) algorithm proposed in [17]. The first step of DARINS is to obtain channel estimates, \hat{H} and compensate the channel distortion

$$\tilde{R}^{(l)}(k) = \frac{S(k)H(k)}{\hat{H}(k)} + \frac{W(k) + I(k)}{\hat{H}(k)}, \quad k = 0, \dots, N - 1 \quad (4.8)$$

where l is iteration loop number. Estimating the channel impulse response in IN channel is another issue that is discussed in next section. The DAR part then comes into play to reduce the IN effect. Making hard-decision on the equalized samples, we obtain $\hat{S}(k)$, $k \in \mathbb{S}$, where \mathbb{S} is a set of data subcarrier indexes. The transmit frequency domain sequence is then reconstructed by inserting virtual carriers and pilot tones, obtaining $\hat{S}(k)$, $k = 0, \dots, N - 1$. Using the reconstructed signal, we estimate the noise

term by

$$\hat{D}^{(l)}(k) = \left(\tilde{R}^{(l)}(k) - \hat{S}^{(l)}(k) \right) \cdot \hat{H}(k), \quad k = 0, \dots, N-1, \quad (4.9)$$

and taking IDFT on $\hat{D}^{(l)}(k)$, $k = 0, \dots, N-1$ to obtain the time domain sequence $\hat{d}^{(l)}(n)$, $n = 0, \dots, N-1$. In order to detect IN-corrupted samples, we use the thresh-

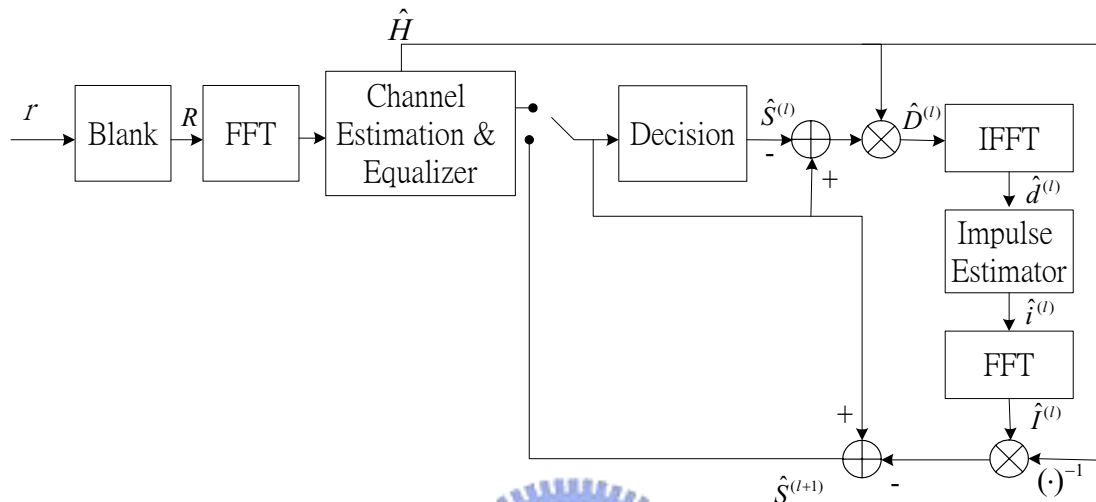


Figure 4.4: Decision-aided reconstruction for impulse noise suppression (DARINS) operation flow.

old

$$T = T_A \cdot \frac{1}{N} \sum_{n=0}^{N-1} \left| \hat{d}^{(l)}(n) \right| \quad (4.10)$$

where T_A is a adjustable threshold. The estimation of impulse noise samples is reconstructed by

$$\hat{i}^{(l)}(n) = \begin{cases} \hat{d}^{(l)}(n), & \text{if } |\hat{d}^{(l)}(n)| > T, \quad n = 0, \dots, N-1 \\ 0, & \text{otherwise} \end{cases} \quad (4.11)$$

The frequency domain IN representation $\hat{I}^{(l)}(k)$, $k = 0, \dots, N-1$ is obtained by taking DFT on $\hat{i}^{(l)}(n)$, $n = 0, \dots, N-1$. Finally, we use $\hat{I}^{(l)}(k)$, $k = 0, \dots, N-1$ to suppress IN,

$$\tilde{R}^{(l+1)}(k) = \tilde{R}^{(l)}(k) - \frac{\hat{I}^{(l)}(k)}{\hat{H}(k)}, \quad k = 0, \dots, N-1. \quad (4.12)$$

Fig. 4.4 shown a block diagram of DAR for IN suppression.

4.6 Iterative channel estimation using DARINS

Many IN suppression methods assume perfect knowledge of the channel state information is available. Unfortunately, this is not the case when IN is present; on the contrary, it is difficult to gain reliable channel information in the presence IN. A better approach is to formulate the problem as one of joint channel estimation and signal detection with nonlinear IN distortion. In this section, we propose an iterative channel estimation procedure that compensates for the IN distortion simultaneously.

When impulse noise is present in the pilot locations, any pilot-assisted channel estimator becomes highly unreliable. A channel estimator that takes impulse noise into account is thus very desirable. The interplay between the INS unit and the channel estimator suggests that an iterative approach that exchange the information provided by each unit may leads to a satisfactory solution. The idea is to use pilots in those symbols that are not corrupted by IN to construct reliable initial channel estimation. Fig. 4.5

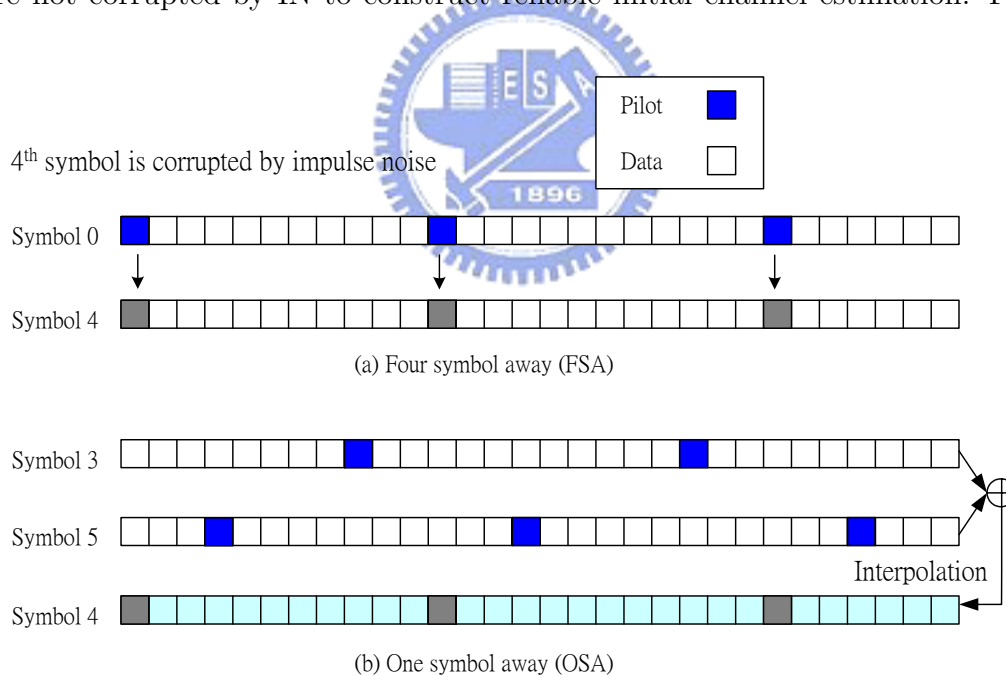


Figure 4.5: Initial channel estimation for DARINS (a) FSA (b) OSA.

(a) is use pilots from the previous symbol with the same pilot location (in DVB-T pilot

period is four symbols). Fig. 4.5 (b) is use pilots from neighboring symbols produce channel estimates using interpolation. The performance of initial channel estimation method 1 (Fig. 4.5 (a)) is worse than method 2 (Fig. 4.5 (b)) since the Doppler frequency is increased. But the performance of method 2 is better than method 1 when the delay spread of channel is increased due to the coherent bandwidth is reduce.

After the initial channel estimation is obtained from method 1 or 2 in Fig. 4.5. We want to have further channel estimation by using iterative operation, thus, iterative channel estimation (ICE). According to equation (4.13), we replace $\hat{H}(k)$ with $\hat{H}^{(1)}(k)$, thus initial channel estimation, and set l equals to one. Now, the equation can be expressed as

$$\tilde{R}^{(1)}(k) = \frac{S(k)H(k)}{\hat{H}^{(1)}(k)} + \frac{W(k) + I(k)}{\hat{H}^{(1)}(k)}, \quad k = 0, \dots, N - 1, \quad (4.13)$$

the procedure is like last section, we make decision on $\tilde{R}^{(1)}(k)$, $k = 0, \dots, N - 1$, then we obtain $\hat{S}^{(1)}(k)$, $k = 0, \dots, N - 1$. The noise term is

$$\hat{D}^{(1)}(k) = \left(\tilde{R}^{(1)}(k) - \hat{S}^{(1)}(k) \right) \cdot \hat{H}^{(1)}(k), \quad k = 0, \dots, N - 1. \quad (4.14)$$

The noise term in time domain is

$$\hat{d}^{(1)}(n) = \text{IFFT}\{\hat{D}^{(1)}\}, \quad n = 0, \dots, N - 1 \quad (4.15)$$

The estimation of impulse noise samples at first iteration is

$$\hat{i}^{(1)}(n) = \begin{cases} \hat{d}^{(1)}(n), & \text{if } |\hat{d}^{(1)}(n)| > T, \\ 0, & \text{otherwise} \end{cases} \quad n = 0, \dots, N - 1 \quad (4.16)$$

The impulse noise frequency response is

$$\hat{I}^{(1)}(k) = \text{FFT}\{\hat{i}^{(1)}\}, \quad k = 0, \dots, N - 1. \quad (4.17)$$

At the end of first iteration we obtain

$$\tilde{R}^{(2)}(k) = \tilde{R}^{(1)}(k) - \frac{\hat{I}^{(1)}(k)}{\hat{H}^{(1)}(k)} \quad k = 0, \dots, N - 1. \quad (4.18)$$

then we extract the scatter pilot tones in $\tilde{\mathbf{R}}^{(2)}$, and use those pilots to re-estimate the channel of current symbol use those channel estimation algorithms mentioned in Chapter 3. After that we acquired a new reliable channel estimation in impulse noise environment, $\hat{\mathbf{H}}^{(2)}, \hat{\mathbf{H}}^{(3)}, \dots, \hat{\mathbf{H}}^{(l)}$. Fig. 4.6 shows our propose system to suppress impulse noise.

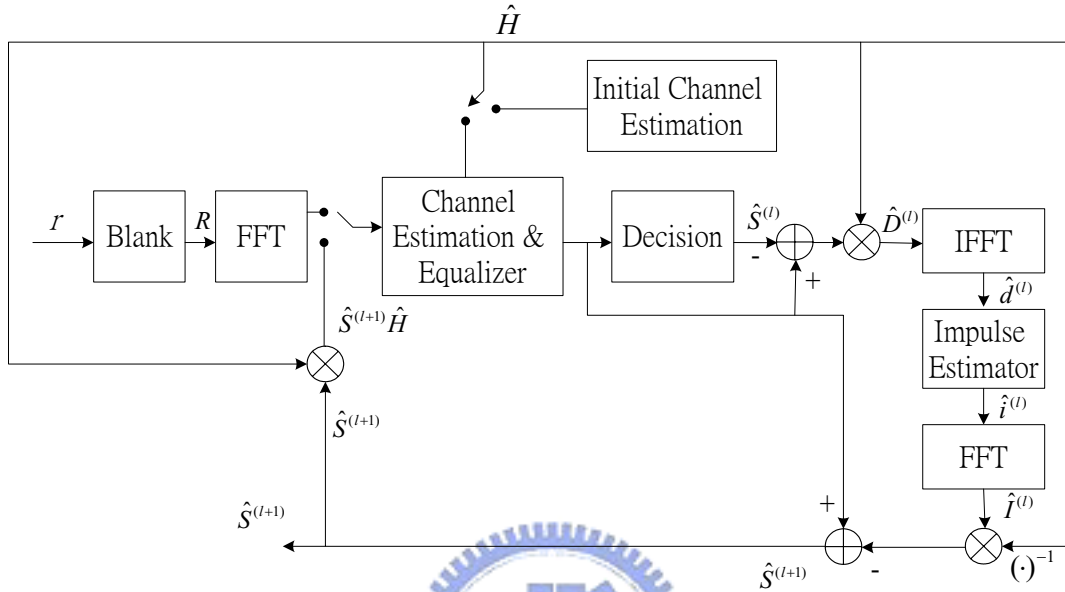


Figure 4.6: The operation flow of propose algorithm. (DARINS with ICE).

4.7 Viterbi approach for impulse noise suppression

In the presence of IN, $i(n)$ and AWGN $w(n)$ the received time domain signal is given by

$$r(n) = s(n) \otimes h(n) + w(n) + i(n), \quad (4.19)$$

Assuming perfect IN detection and blanking, we expressed the resulting samples as

$$r_b(n) = \begin{cases} 0 & n \in \mathcal{D} \\ s(n) \otimes h(n) + w(n) & \text{otherwise} \end{cases} \quad (4.20)$$

or equivalently,

$$r_b(n) = s(n) \otimes h(n) + w(n) - \text{rect} \left(\frac{n - n_0}{|\mathcal{D}|} \right) \cdot \{s(n) \otimes h(n) + w(n)\}. \quad (4.21)$$

where \mathcal{D} is the set of those samples corrupted by impulse noise and $|\mathcal{D}|$ is the cardinality of \mathcal{D} . Transforming 4.21 into the frequency domain, we obtain

$$R(k) = S(k)H(k) + W(k) - \sum_{\tau=-N}^{N-1} (S(\tau)H(\tau) + W(\tau))\Lambda(\tau - k) \quad (4.22)$$

$$= S(k)H(k) - \sum_{\tau=-N}^{N-1} S(\tau)H(\tau)\Lambda(\tau - k) + W'(k) \quad (4.23)$$

$$= S(k)H(k)(1 - \Lambda(0)) - \sum_{\tau=-N, \tau \notin \mathcal{D}}^{N-1} S(\tau)H(\tau)\Lambda(\tau - k) + W'(k) \quad (4.24)$$

where $\{\Lambda(k)\}$ is Fourier transform of the rectangular function $\lambda(n)$ which is nonzero and has unit magnitude only if $n \in [0, (|\mathcal{D}|)]$. Define

$$\Lambda'(m) = \begin{cases} 1 - \Lambda(0) & m = 0 \\ -\Lambda(m) & \text{otherwise} \end{cases} \quad (4.25)$$

we obtain a simplified version of (4.22)

$$R(k) = \sum_{\tau=-N}^{N-1} S(\tau)H(\tau)\Lambda'(\tau - k) + W'(k) \quad (4.26)$$

Noted that $R(k)$ in (4.26) is similar to a ISI-corrupted sequence, hence one can use the Viterbi algorithm to solve for $S(\tau)$ given the channel response $H(\tau)$ is known. However, such a formulation results in a trellis with a large number of states. Some reduced-state algorithm might be helpful in making this approach a practical one.

4.8 Computational complexity

Our proposed impulse-noise-suppression, DARINS, need to $2N$ storage for $\hat{S}^{(l)}$ and $\hat{H}^{(l)}$, and it requires $2N$ complex division and N complex multiplication for equalization for every iteration. Each iteration requires N points FFT and N points IFFT. It needs $N \log_2 N$ complex multiplication for FFT and IFFT operation. DARINS needs N addition for calculate the noise term and N addition for obtain estimation of signal. Final, it requires N addition to obtain the threshold T , see (4.10).

4.9 Simulation and numerical examples

The proposed impulse noise suppression algorithm (DARINS+ICE) is evaluated under Rayleigh fading channel with impulse noise. In following simulation results, we use 2-D regression channel estimation (regres.(3,3)) with TDP that we proposed in Chapter 3. Of course, we can use LS or other channel estimation algorithms. In Fig. 4.7, it is simulate in static Rayleigh fading channel and only received one station's signal (shorter delay spread) and impulse noise is occurred exactly every 8 symbol. We can see that in Fig. 4.7, by using the blanking method can reduce a little impulse noise influence. When use DARINS, we can obtain more improvement than blanking method. Both 4.5 FSA or OSA can obtain a good channel estimation for the symbol corrupted by impulse noise, because channel is static. Therefore, iterative channel estimation (ICE) can not obtain more improvement. Fig. 4.9 is a different situation, the channel is fast fading and coherent bandwidth is narrower. Both 4.5 FSA or OSA initial channel estimation is unreliable, because the channel estimation of other symbol is quiet different when channel is fast fading. Therefore, iterative channel estimation (ICE) can provide a better channel estimation by recursive update.

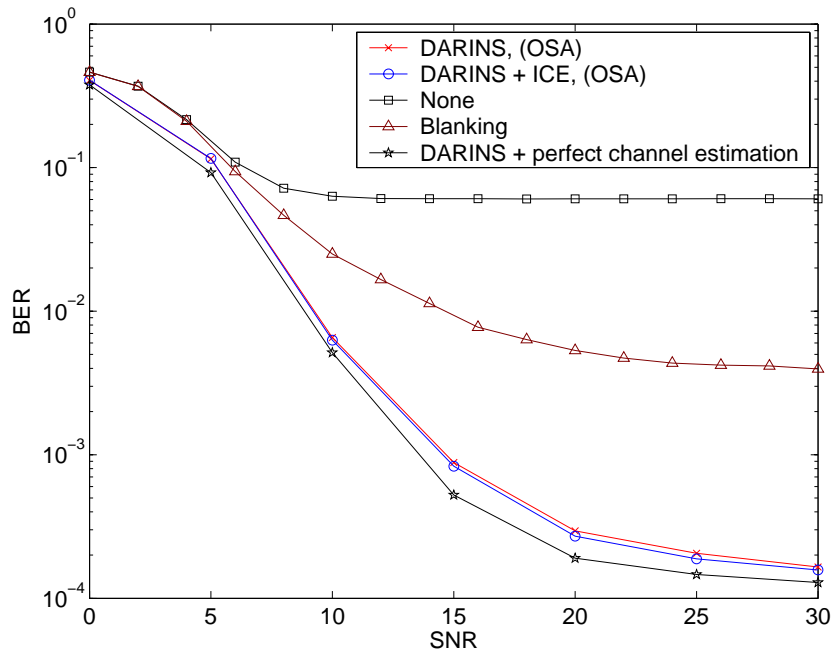


Figure 4.7: QPSK modulation, code rate is $\frac{1}{2}$ in DVB-T Rayleigh fading channel with impulse noise (Cook pulse). Iteration 3 times. regres. (3,3). Doppler frequency $0Hz$. r.m.s. delay spread $1.36\mu s$ (12.5 OFDM sample).

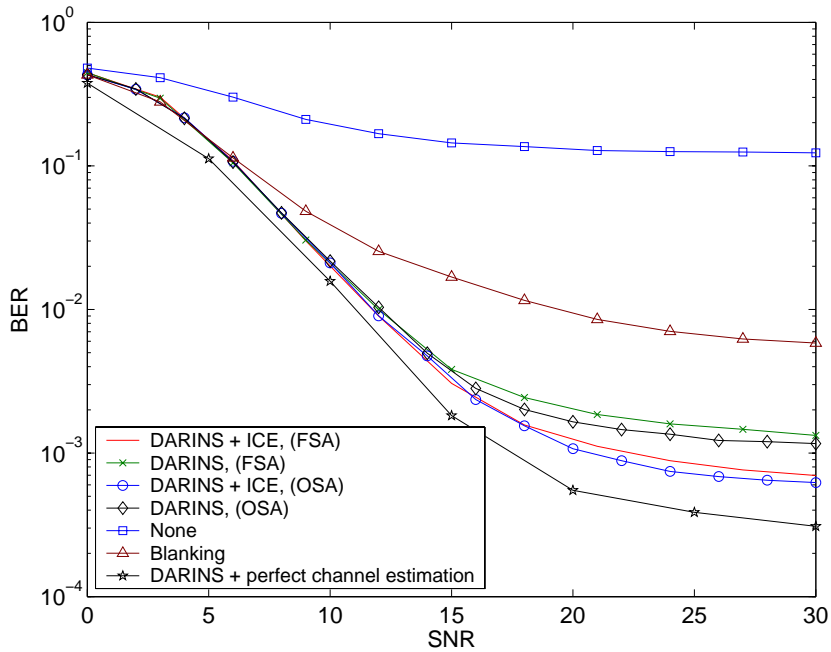


Figure 4.8: QPSK modulation, code rate is $\frac{1}{2}$ in DVB-T Rayleigh fading channel with impulse noise (Cook pulse). Doppler frequency from $44Hz$. r.m.s. delay spread $5.13\mu s$ (48 OFDM sample).

Chapter 5

Baseband Architecture

In this chapter we propose an overall baseband receiver for DVB-T systems based on the algorithms we developed earlier. Figs. 5.2, 5.3, 5.4, 5.5 and 5.6 plot various subsystem architectures of the proposed DVB-T baseband receiver. The overall architecture is given in Fig. 5.1 in which the received analog signal is converted by ADC then the sampled sequence is forwarded to the IN detector. If an IN arrival is detected, the IN detector will send a message to enable IN blanking and the receiver will switch to the IN mode. Otherwise, the IN blanking circuitry remains idle and the receiver stays at the regular mode. Coarse timing synchronizer gives the coarse timing information to the FFT window controller, and then based on this estimator, we remove samples in the guard interval and send the remaining samples to the FFT block.

After performing FFT and removing guard band samples, we save those useful samples to RAM for further processing. The frequency synchronization unit then uses continual pilots to estimate the coarse frequency offset. The resulting estimate is used for frequency offset compensation, and the loop (synchronization) lock detector monitors the synchronizer's locking state to enable the micro-control to activate and de-active a particular synchronization unit. Because the 2D model-based channel estimation needs 7 symbols at least. The corresponding memory management is crucial in saving the memory space. When the 2D-MB-TDP estimator obtains a symbol's channel information it sends this information for equalization to eliminate channel effect immediately.

On the other hand, timing tracking starts operating when LS channel estimation is done, see Fig. 5.5. If the IN detector detects the presence of IN and outputs an IN-on signal to ICE and initial channel estimator, which then activate the 2D-MB-TDP algorithm and the iterative channel estimation procedure as well. The IN detector is also responsible for checking if DARINS is working properly.

As just mentioned, the Lock loop detector is in charge of monitoring the other timing error and frequency synchronization units. When timing error or frequency offset is out of locked-in range so that tracking circuitry is not capable of providing accurate updated information, the lock detector sends an alarm message to the synchronization controller, indicating that a re-acquisition or re-synchronization process should be initialized.

Based on Texas Instruments' product, TMS320C6701 DSP, we estimate the required operation time of our proposed algorithms. The cycle time of TMS320C6701 is $6ns$, and an additive operation needs only 1 cycle, a real multiplicative needs 2 cycles i.e. $12ns$. Now, the environment for calculating operation time is DVB-T 2K mode, guard interval is 128 samples, $N_g = 128$. We assume a complex multiplication needs 3 additions and 4 multiplications. Coarse timing will need $6N_g$ additions and $8N_g$ multiplications, thus needs $16.89 \cdot 10^{-6}$ seconds for calculate $\hat{\theta}$. A symbol period is $238\mu s$, useful part $224\mu s$ and guard interval $14\mu s$. The total operation time of coarse timing synchronization for one symbol is $254\mu s$. Fine frequency offset estimation needs $4N_G$ additions and $5N_G$ real multiplications every symbol, i.e. $10.7 \cdot 10^{-6}$. There are 45 continual pilots in the 2K mode i.e. $N_{cp} = 45$. Coarse frequency offset synchronization needs N_{cp} additions and N_{cp} multiplications for each time we calculate ϕ_m . It needs $0.54 \cdot 10^{-6}$ seconds for each time. We assume that search region of ϕ_m from -10 to 10, it requires calculate ϕ_m 21 times, the coarse frequency offset estimation is $11.34 \cdot 10^{-6}$. Timing tracking needs $N_p - 1$ addition and multiplication, that's $1.716 \cdot 10^{-6}$. 2D-MB-TDP requires 4 complex multiplication per subcarrier i.e. $12N$ additions and $16N$ real multiplications for a symbol. 2D-MB-TDP needs $9.83 \cdot 10^{-5}$ seconds. DARINS is require very large

computational complexity, each iteration needs more than $392\mu s$ operation time. Fig. 5.7 shown the overall execution time, symbol 0 to symbol 2 is regular mode and symbol 9 to 10 is impulse noise mode (IN mode). In the IN mode, the DARINS algorithm has to operate over two more symbol periods because the related FFT operation requires relative high complexity.



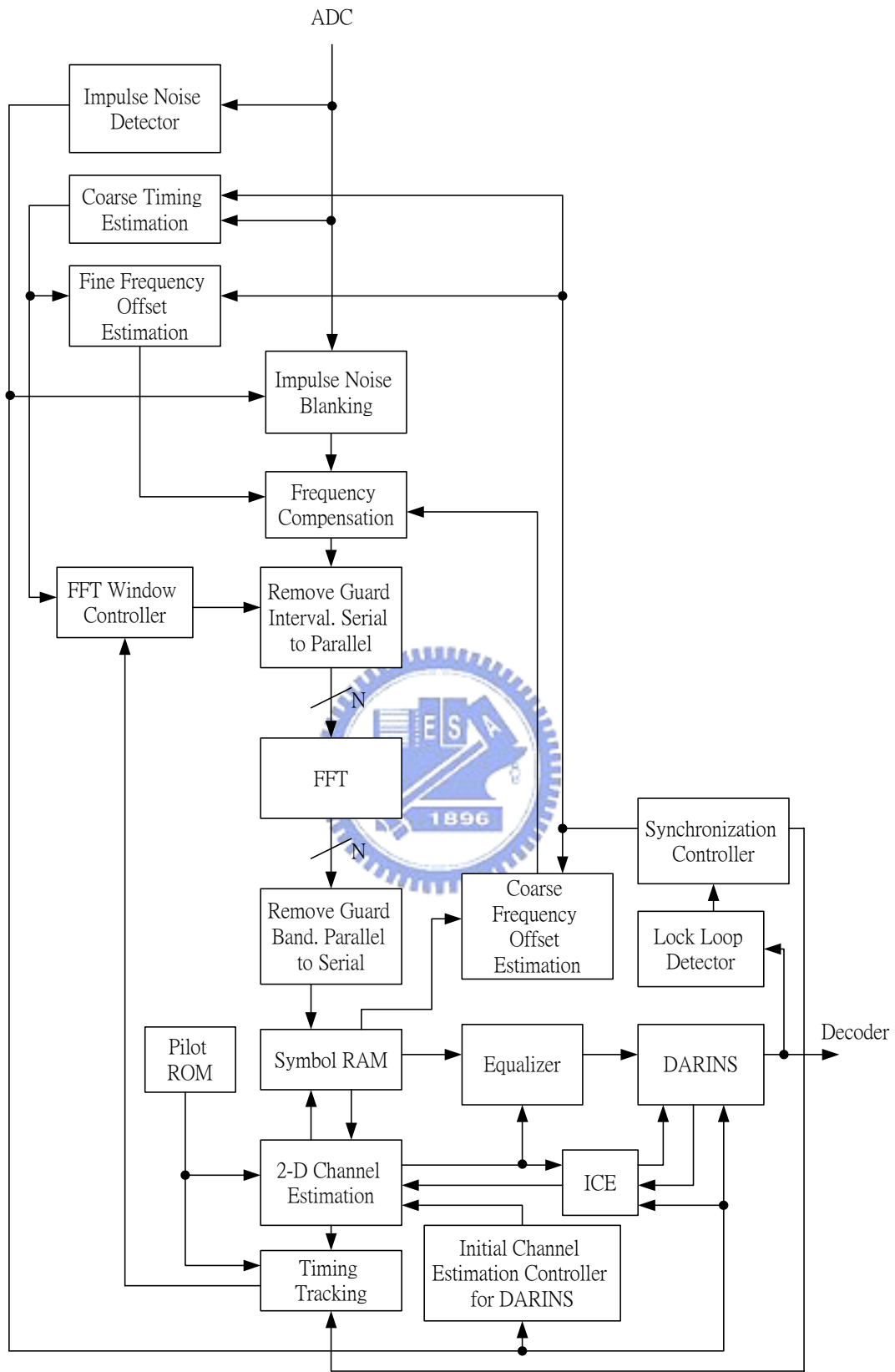


Figure 5.1: Proposed DVB-T baseband receiver architecture.

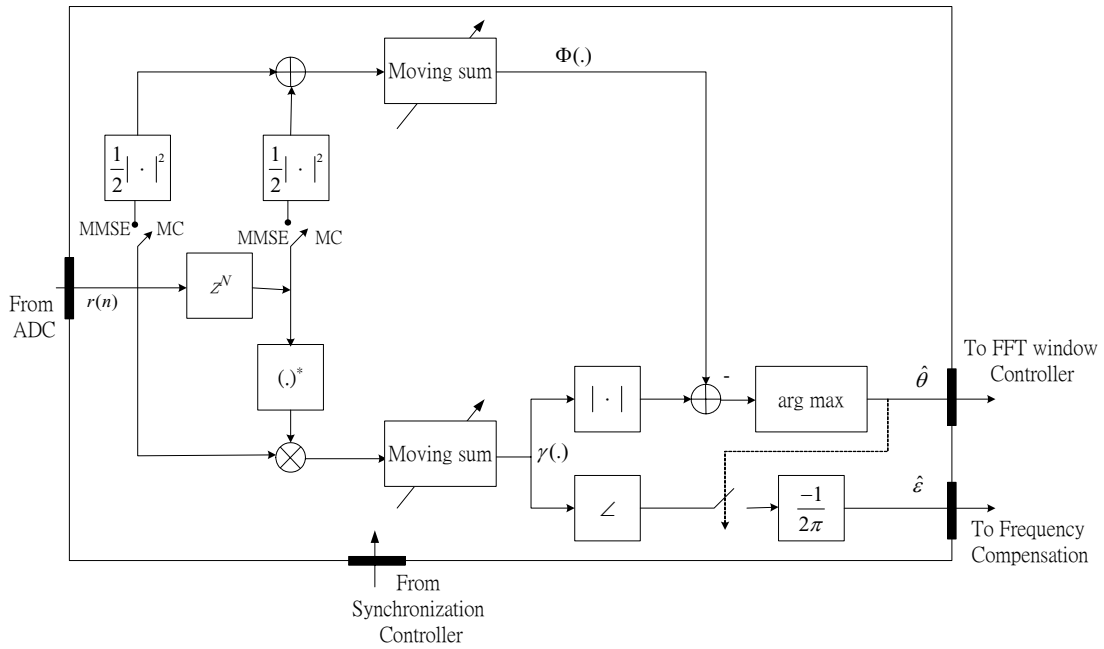


Figure 5.2: The architecture of the coarse timing and fine frequency offset synchronization unit.

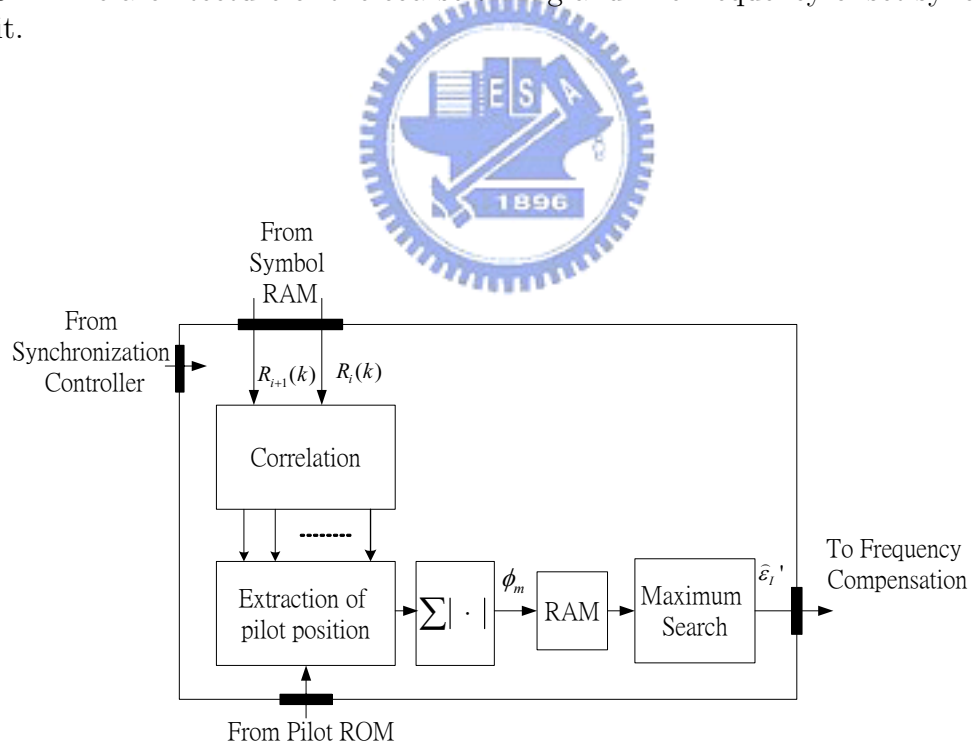


Figure 5.3: The architecture of the coarse frequency offset synchronization unit.

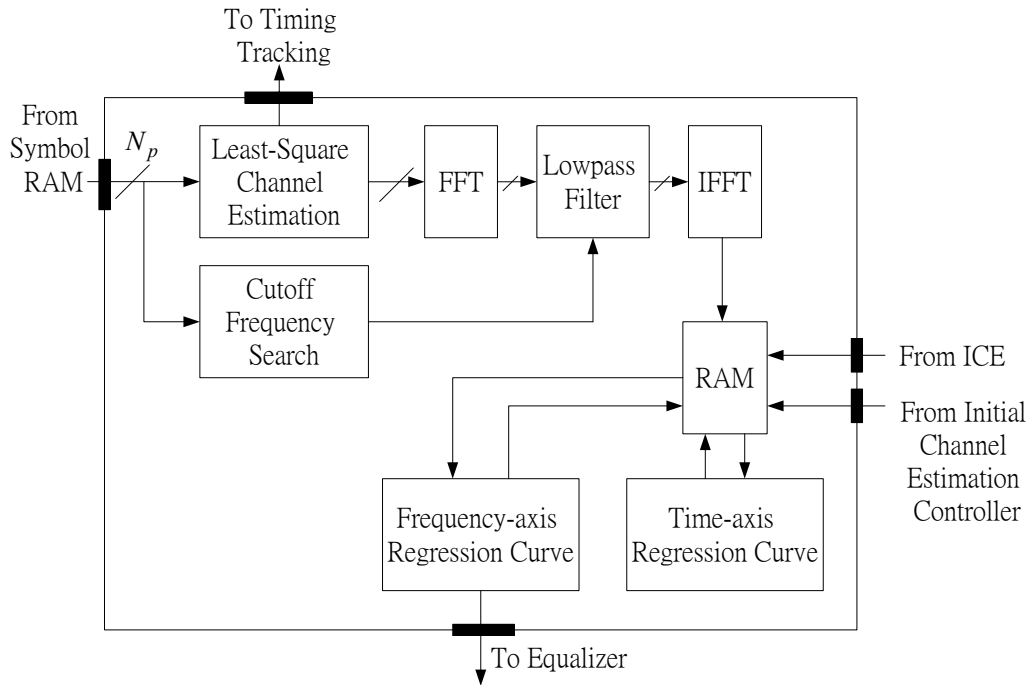


Figure 5.4: The architecture of the 2D model-based channel estimator with transform-domain processing.

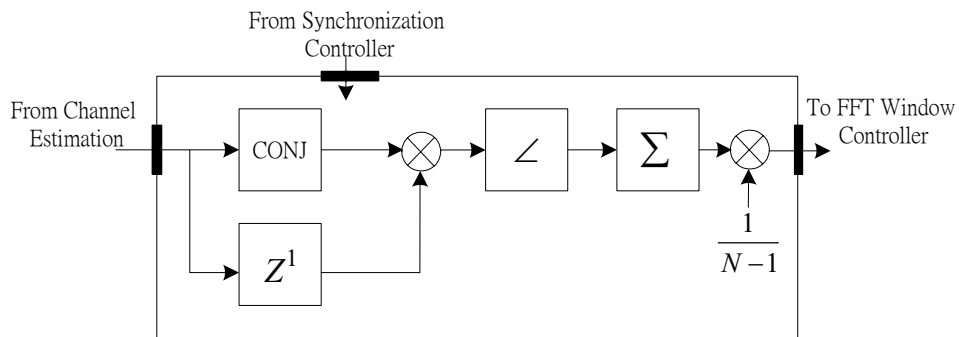
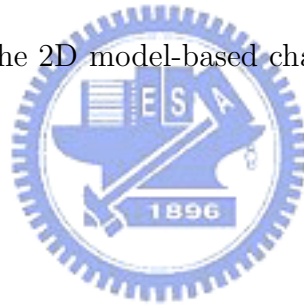


Figure 5.5: Architecture of the timing tracking unit.

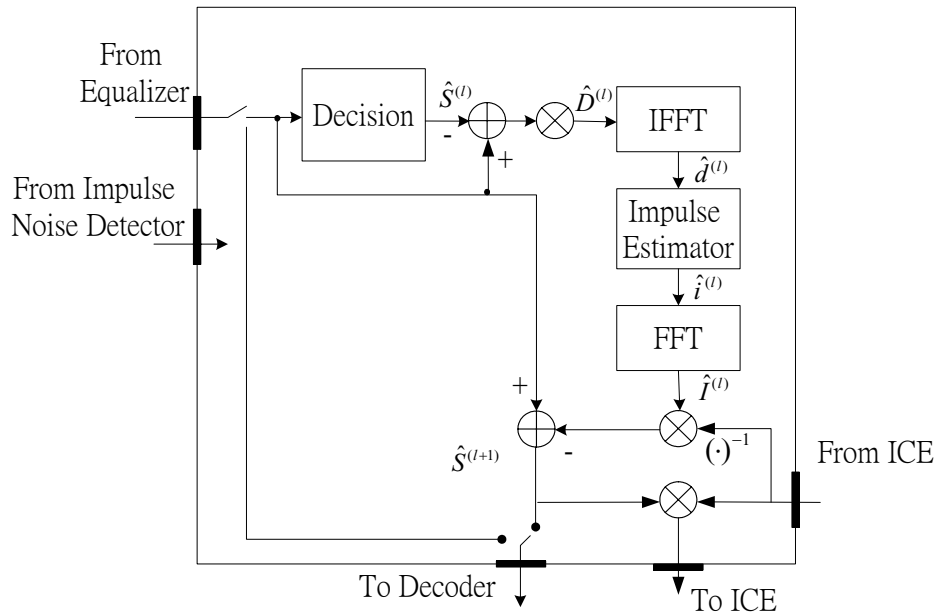


Figure 5.6: Block diagram showing the architecture for the DARINS with ICE algorithm.

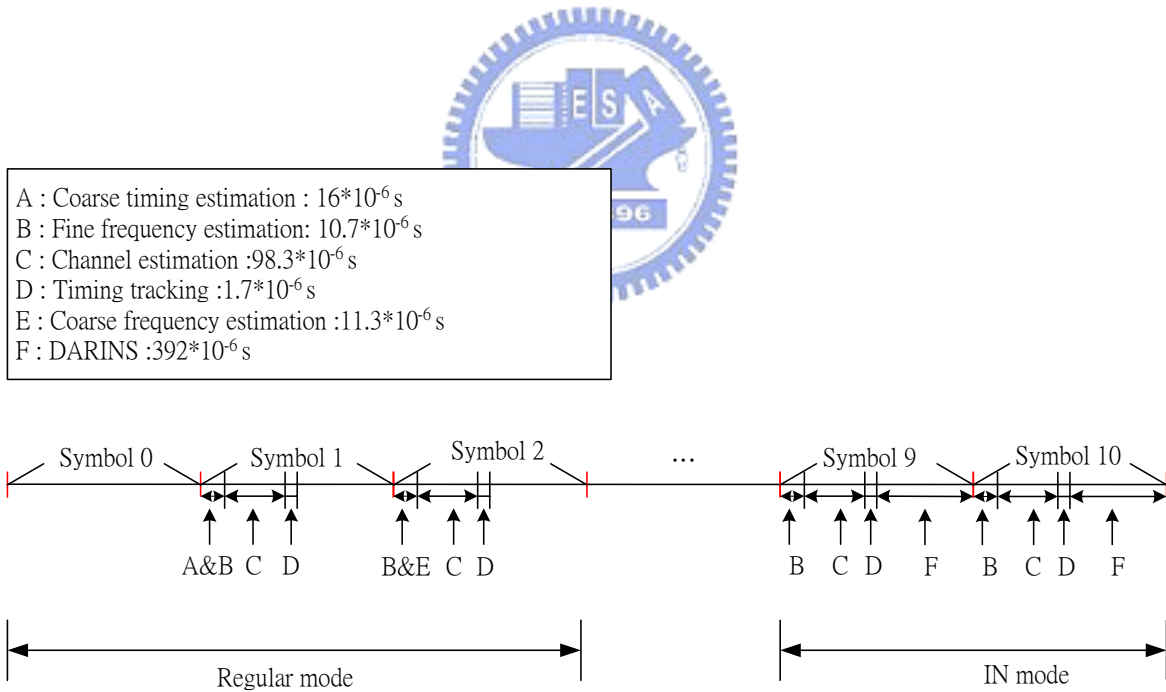


Figure 5.7: An estimation of the overall system execution time, symbol 0 to symbol 2 is in the regular mode while symbol 9 to 10 is in the IN (impulse noise) mode.

Chapter 6

Conclusion

In this thesis, we have investigated and developed algorithms associated with various baseband subsystems within the inner receiver. Numerical examples are given to validate and compare the performance of the proposed algorithms. We proposed a fast coarse frequency offset synchronizer with excellent performance. This algorithm also requires less samples in computing the estimate. We have addressed issues concerning the complete synchronization procedure include coarse timing synchronization, coarse and fine frequency synchronization, and fine timing tracking. We also examine three different channel estimation algorithms using scatter pilot and propose a 2-D regression channel estimate with transform-domain pre-processing, using four or more symbols. This algorithm is robust in both SFN (longer delay spread) scenario and mobile channel (larger Doppler frequency). simpler 1-D channel estimates, LS or TDP, work for static channels with smaller delay spread.

Finally we present a feasible solution for IN suppression and provide an iterative solution for simultaneous channel estimation and IN suppression, saving the system performance from serious deterioration. The latter iterative solution, however, requires relatively high complexity and therefore calls for further simplification in the future.

Bibliography

- [1] *ETSI, Digital Video Broadcasting (DVB); Framing structure, channel coding and modulation for terrestrial television, ETS 300 744, March 1997.*
- [2] *Wireless LAN Medium Access Control (MAC) and Physical Layer (PHY) Specifications, In IEEE Std 802.11-1999, 1999.*
- [3] D. Lee and K. Cheun, “Coarse symbol synchronization algorithms for OFDM systems in multipath channels,” *IEEE Commun. Letter*, vol. 6, No. 10, Oct. 2002.
- [4] T. Keller and L. Hanzo, “Orthogonal frequency division multiplex synchronization techniques for wireless local area networks,” in *Proc. IEEE PIMRC’96*, Oct. 1996, pp. 963-967.
- [5] M. Speth, F. Classen, and H. Meyr “Frame synchronization of OFDM systems in frequency selective fading channels,” in *Proc. IEEE Vehi. Tech. Conf.*, May 1997, pp. 1807-1811.
- [6] J.-J. van de Beek, M. Sandell, and P. O. Borjesson, “ML estimation of time and frequency offset in OFDM systems,” *IEEE Trans. Signal Processing*, vol. 45, pp. 1800-1805, July 1997.
- [7] D. Han, J. Seo and J. Kim, “Fast carrier frequency offset compensation in OFDM systems,” *IEEE Trans. on Consumer Elec.*, vol. 47, No. 3, Aug. 2001.
- [8] S. Kay, “A fast and accurate single frequency estimator,” *IEEE trans. ASSP.*, vol. 37, no. 12, Dec. 1989.

- [9] J. Rinne and M. Renfors, "Pilot spacing in orthogonal frequency division multiplexing systems on practical channels," *IEEE Trans. Consumer Elec.*, vol. 42, no. 4, Nov. 1996.
- [10] W. C. Jakes, *Microwave Mobile Communizations*, IEEE press, 1993.
- [11] Y. Zhao and A. Huang, "A novel channel estimation method for OFDM communication systems based on pilot signals and transform-domain processing," in *Proc. IEEE 47th Veh. Tech. Conf.*, Phoenix, USA, May 1997, pp. 2089-2093.
- [12] M. X. Chang and Y. T. Su, "Model-based channel estimation for OFDM signals in Rayleigh fading," *IEEE trans. on commun.*, vol. 50, n0. 4, April 2002.
- [13] M. Sliskovic, "Signal processing algorithm for OFDM channel with impulse noise," in *Proc. of ICECS'00*, Jounieh, Lebanon, pp. 222-225, Dec. 2000.
- [14] M. Ghosh, "Analysis of the effect of impulse noise on multicarrier and single carrier QAM systems," *IEEE Trans. on Commun.*, vol. 44, no. 2, Feb. 1996.
- [15] M. Sanchez, L. Haro and M. Romon, "Impulsive noise measurements and characterization in a UHF digital TV channel," *IEEE Tran. on Elec. Comp.*, vol. 41, no. 2, May 1999.
- [16] K. T. Foster and J. W. Cook, "A symbolic pulse for impulsive noise testing," in *ANSI T1E1.4 Commun. Cont.*, no.92-143, OR, August 1992.
- [17] D. Kim and G. J. Stuber, Clipping noise mitigation for OFDM by decision-aided reconstruction, *IEEE Commun. Letters*, vol. 2, no. 5, May 1998.

簡 歷

姓 名：黃俊傑

居 住 地：台北縣

出生年月日：民國六十九年八月二十九日

學 經 歷：

高雄科技學院電子工程科 (87年9月~89年6月)

台灣科技大學電子工程系 (89年9月~91年6月)

交通大學電信工程學系碩士班 (91年9月~93年6月)

Graduate Course：

Digital Communication
Random Process
Digital Signal Processing
Detection and Estimation Theory
Digital Communication Receiver
Array Signal Processing
Adaptive Signal Processing
Digital Signal Processing Project

